

Tide2Topo: A new method for mapping intertidal topography accurately in complex estuaries and bays with time-series Sentinel-2 images

Chunpeng Chen^{a,b}, Ce Zhang^{b,c,*}, Bo Tian^{a,*}, Wenting Wu^d, Yunxuan Zhou^a

^a State Key Laboratory of Estuarine and Coastal Research, East China Normal University, Shanghai 200241, China

^b Lancaster Environment Centre, Lancaster University, Lancaster LA1 4YQ, UK

^c UK Centre for Ecology & Hydrology, Library Avenue, Lancaster LA1 4AP, UK

^d Key Laboratory of Spatial Data Mining and Information Sharing of Ministry of Education, National & Local Joint Engineering Research Center of Satellite Geospatial Information Technology, Fuzhou University, China

ARTICLE INFO

Keywords:

Intertidal topography
Tide inundation
Time-series
Sentinel-2

ABSTRACT

Intertidal zones serve as a critical transition between land and ocean and are periodically inundated by tides. They are extremely important to coastal communities as it provides diverse habitats and buffers against marine hazards. However, the reduced river sediment together with sea level rise and coastal reclamation have caused the widespread loss of intertidal areas. Reliable, high-resolution, and up-to-date intertidal topography maps are key information for coastal vulnerability assessment and restoration. Existing approaches to intertidal topography reconstruction involve significant ground surveys, with limited spatial coverage, accuracy, and efficiency, thus, restricting their potential to generalize globally. To address these issues, we propose a pixel-based approach to construct intertidal topography from dense Sentinel-2 satellite time-series and limited ground truth surveys, named as Tide2Topo. Tide2Topo differs conceptually from the widely used waterline method since it considers tidal inundation frequency as a topographic indicator rather than instantaneous waterlines. Therefore, Tide2Topo does not involve manual selection of images at different tide levels. The relationship between intertidal inundation frequency and elevation is calibrated using linear and polynomial models based on a few transect measurements instead of tidal height, preventing errors introduced by inaccurate tidal data. The proposed Tide2Topo was applied and validated in the UK and China over several complicated estuaries and bays with extensive muddy flats or sandy beaches. The results demonstrated that the topography derived from intertidal inundation frequency compared to LiDAR or UAV photogrammetric observations has a root mean square error ranging from 16 to 38 cm. The large errors were found in the tidal channel areas where the inundation frequency calculation was prone to uncertainty. Dense Sentinel-2 time-series observations ensure finer sampling of the tidal cycle, thereby not only eliminating errors caused by spatial interpolation but also maintaining the accuracy of elevation estimations at pixel level. Tide2Topo is a robust, portable and rapid method that is well suited to large-scale intertidal topography reconstruction. Future work could use Sentinel-1 SAR as an alternative data source for Tide2Topo, realizing seasonal or annual monitoring of intertidal geomorphological changes.

1. Introduction

Intertidal zones can range from steep rocky cliffs to gently sloping sandy beaches and mudflats extending over hundreds of meters, and are periodically inundated by tides. They are of great social, economic and environmental significance due to their ability to support biodiversity hotspots (Loke and Todd, 2016), mitigate coastal erosion (Temmerman et al., 2013), protect coastal communities from marine hazards (Morris et al., 2018), and provide ample land resources (Nienhuis et al., 2020).

However, accelerated sea-level rise, rapid decrease in river sediments, and extensive coastal reclamation have led to a considerable loss, degradation, and fragmentation of these tidal environments globally (Hill et al., 2021; Murray et al., 2022; Wu et al., 2022). To understand the impact of these stresses on tidal environments and to establish priority protection and implement restoration, intertidal topography needs to be updated frequently with accuracy. However, intertidal topography remains poorly captured due to limited accessibility and short duration of exposure. Even existing global digital elevation models (DEMs) (e.g.,

* Corresponding authors.

E-mail addresses: c.zhang9@lancaster.ac.uk (C. Zhang), btian@sklec.ecnu.edu.cn (B. Tian).

<https://doi.org/10.1016/j.isprsjprs.2023.05.004>

Received 6 November 2022; Received in revised form 26 February 2023; Accepted 4 May 2023

Available online 10 May 2023

0924-2716/© 2023 The Author(s). Published by Elsevier B.V. on behalf of International Society for Photogrammetry and Remote Sensing, Inc. (ISPRS). This is an open access article under the CC BY license (<http://creativecommons.org/licenses/by/4.0/>).

the Shuttle Radar Topography Mission (SRTM) and the Advanced Spaceborne Thermal Emission and Reflection Radiometer (ASTER) suffer from either gaps in data or unacceptable errors (Kulp and Strauss, 2018; Zhang et al., 2019).

Intertidal topographic mapping commonly refers to the construction of topography in non-vegetated areas, as the dense salt marsh vegetation (e.g., *Spartina alterniflora* and *Phragmites australis*) in the supratidal zone brings additional challenges to access the topography beneath the vegetation directly. The intertidal topography construction depends largely on remote sensing techniques given the highly specific geographical environment and is mostly conducted in combination with *in-situ* observations (Bell et al., 2016; Bishop-Taylor et al., 2019; Ryu et al., 2008). These technologies can be broadly categorized into three types: ground-based, airborne-based, and spaceborne-based surveys. Ground-based (e.g., terrestrial laser scanning) and airborne-based (e.g., aerial photogrammetry and aerial LiDAR) measurements can provide highly accurate surface elevation of intertidal zones (Andriolo et al., 2018; Chen et al., 2022a; Huff et al., 2019; Xie et al., 2017). However, they are considerably restricted by the limited spatial coverage, high economic costs, and low efficiency, thereby large-scale intertidal topography is challenging to establish. In contrast, spaceborne-based observations have the advantages of abundant data sources, large spatial coverage, and high temporal frequency (Bergsma et al., 2021; Salameh et al., 2019), and are more appropriate for constructing intertidal topography at a large scale.

Current spaceborne-based techniques for mapping intertidal topography include interferometric synthetic aperture radar (Lee and Ryu, 2017), satellite radar altimetry (Salameh et al., 2021), remotely sensed soil moisture approach (Li et al., 2022), and waterline method (Mason et al., 1995). Amongst them, the waterline method is the most commonly used approach due to its simple operation, easy access to data, and high stability in comparison with other methods (Bell et al., 2016; Heygster et al., 2010; Salameh et al., 2020; Yamano et al., 2006). The waterline method implementation involves three steps, including waterline delineation, elevation assignment of waterlines, and topography interpolation. Each step could result in errors and uncertainties (Mason et al., 2001). The accuracy of the constructed DEMs depends on the density and quality of waterlines derived from satellites and the accuracy of the tidal height (Tong et al., 2020; Wang et al., 2019). Previous studies have developed several algorithms to minimize errors in waterline extraction, including threshold-based (Sagar et al., 2017; Tong et al., 2020), edge detection-based (Li et al., 2014; Salameh et al., 2020), subpixel-based (Bishop-Taylor et al., 2021; Vos et al., 2019), and deep learning-based methods (Seale et al., 2022; Zhang et al., 2022). These approaches, however, have disadvantages of algorithm stability, accuracy, and automation, especially in the context of spatial heterogeneity imposed by complex coastal types and time-varying tides. In addition, the waterlines generated by the above methods are often discontinuous and fragmented (Yang et al., 2022), requiring extensive manual modifications. Tidal heights used to calibrate instantaneous waterlines tend to be inaccurate as they are simply interpolated from nearby tidal stations or simulated by tidal models. Given these limitations, the waterline method is not the ideal method to construct intertidal topography rapidly at a large scale.

Recently, the use of full time-series satellite observations to study tidal landscapes, empowered by the Google Earth Engine (GEE) cloud computing platform, has become a new paradigm. For example, Cao et al. (2020) and Jia et al. (2021) delineated the spatial extent of tidal flats at a national scale with full time-series Landsat and Sentinel-2 data, respectively. They assumed that dense satellite observations could acquire images at the highest and lowest tides. Similarly, this hypothesis implies that full time-series observations can acquire images at all moments of tidal height within the tidal range. Traditional waterline method uses manually selected images and does not make use of full time-series observations across the whole tidal range. Furthermore, to better understand coastal processes, many intertidal zones involve

regional fine-scale topographic observations using real-time kinematic (RTK) surveys, LiDAR, and unmanned aerial vehicle (UAV) photogrammetric measurements (Bertels et al., 2011; Brunier et al., 2020; Tan et al., 2020). Nevertheless, few studies have combined these local ground truth surveys with satellite observations to generate large-scale intertidal topography. Based on these observations, a new approach to constructing intertidal topography using full time-series satellite observations and local ground truth surveys was developed in this paper.

Here, we present a pixel-based approach, Tide2Topo, to construct intertidal topography from full time-series Sentinel-2 and limited ground truth surveys. The Tide2Topo differs conceptually from the waterline method in that it considers tidal inundation frequency derived from the Sentinel-2 time-series as a topographic indicator rather than instantaneous waterlines. The relationship between intertidal inundation frequency and elevation is calibrated using regression models based on a few transect measurements from LiDAR or UAV photogrammetry instead of tidal heights. Several complex estuaries and bays with extensive muddy flats or sandy beaches in the UK and China were employed to assess and validate the performance of the proposed Tide2Topo approach comprehensively.

2. Study area and datasets

2.1. Study area

We selected the Northwest coast and East coast of England and two typical China intertidal regions as study areas (Fig. 1). These areas are geographically characterized by estuaries and bays with extensive muddy flats, sandy beaches, and sandbanks. These coasts are typical and sufficiently diverse to evaluate the performance of the proposed method. The intertidal zone on the Northwest coast of England comprises several estuaries and bays, largely, including Solway Estuary, Morecambe Bay, Ribble Estuary, and Dee Estuary. The sediments in these estuaries and bays consist predominantly of very fine and fine sand, forming extensive intertidal sand banks and a few muddy flats (Mason et al., 2010). The tide on the Northwest coast of England is semi-diurnal, with a tidal range between around 8 m and 4.4 m with moderate waves (Van Der Wal et al., 2002). The Wash Bay and Thames Estuary, on the East coast of England, include extensive fine sands and drying banks of coarse sand. The intertidal zone is macro-tidal with a tidal range within 5.3 m; the waves within the intertidal zone are relatively small, with a mean annual wave height of 1 m (Van der Wal and Pye, 2004). Sediment characteristics in the Wash Bay and the Thames Estuary differ along the seaward side (Rossington and Spearman, 2009). The inner shore is dominated by fine muddy sediments, whereas the sediments on the outer shore are largely sandy, generating several large sandbanks. In contrast, the east of Chongming Island at the mouth of the Yangtze River and Sansha Bay in Fujian Province, China largely consist of muddy flats. These tidal environments support several biodiversity hotspots and are therefore well recognized as globally important Ramsar wetlands.

2.2. Sentinel-2 data and pre-processing

The Sentinel-2 mission, including twin polar-orbiting satellites (Sentinel-2A and Sentinel-2B commissioned), can provide a wide-swath, high-resolution multispectral imaging mission with a global 5-day revisit interval. 5,005 Sentinel-2 Level-2A surface reflectance images acquired from January 1, 2020 to December 31, 2021 were used in consideration of the high frequency of cloud cover in coastal areas and to obtain Sentinel-2 images with a full tidal range as much as possible (Fig. 2). The scene-level cloud percentage was calculated using the CLOUDY_PIXEL_PERCENTAGE property in the image metadata, and a threshold of 70% was recommended in previous studies (Ni et al., 2021; Tian et al., 2020). Considering that cloud removal algorithms perform poorly on images with high proportions of cloud coverage (Coluzzi et al., 2018), and that image filtering discovered that removing images with

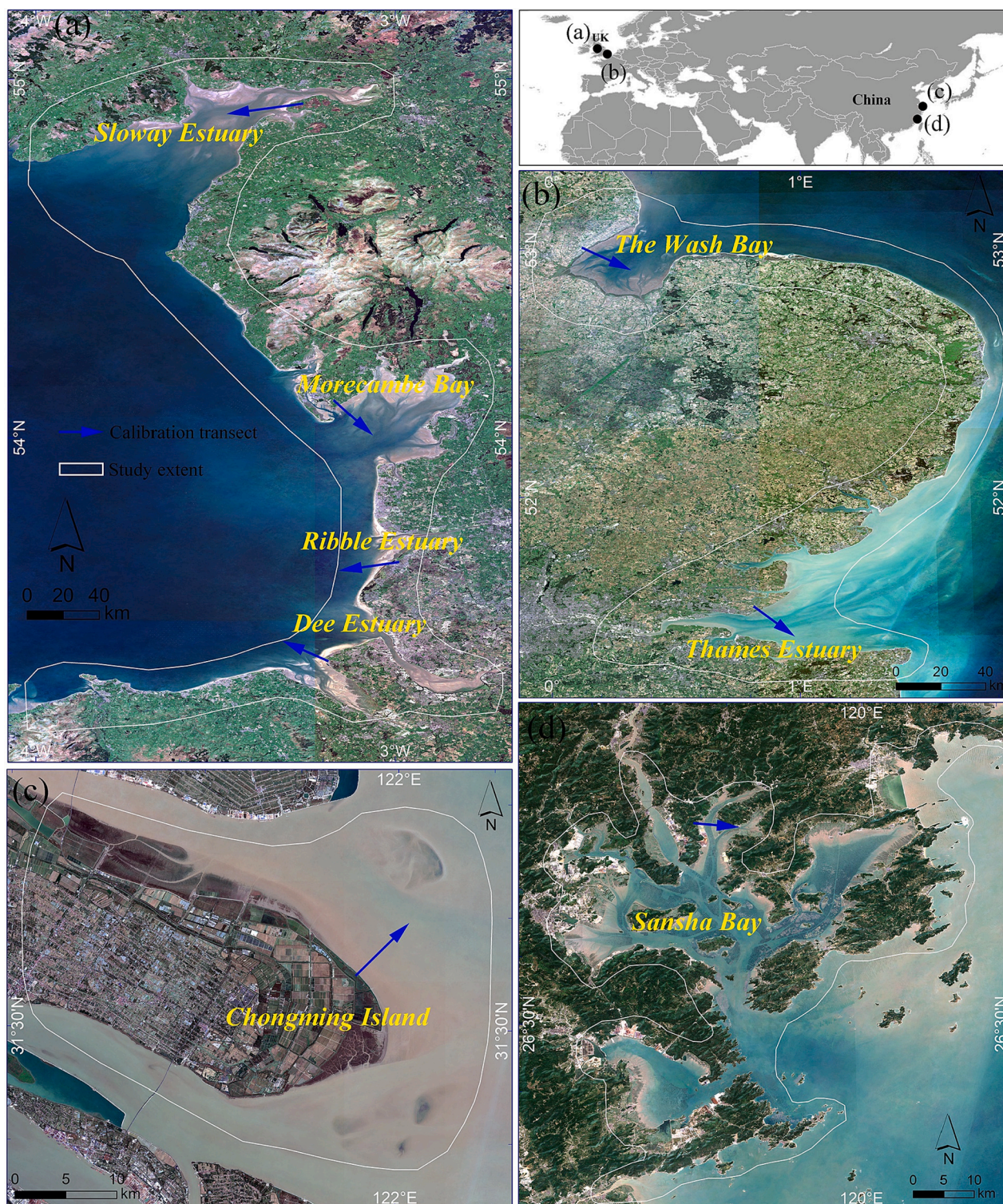


Fig. 1. Maps of the study area for intertidal zones in (a) the northwest coast of England (NWE) with three major estuaries (i.e., Solway Estuary, Ribble Estuary, and Dee Estuary) and one large bay (i.e., Morecambe Bay); (b) the east coast of England (ECE) with the Wash Bay and Thames Estuary; (c) the east of Chongming Island in Yangtze Estuary, China; and (d) Sansha Bay in the northeast of Fujian province, China. The LiDAR or UAV photogrammetric observation sections are shown in the figure by blue arrows. (For interpretation of the references to color in this figure legend, the reader is referred to the web version of this article.)

cloud percentages between 60 and 70% did not significantly reduce the total number of images. Therefore, Sentinel-2 images with a cloudy percentage greater than 60% were excluded in this study. Next, the QA60 bitmask band was used to mask cloudy pixels and generate cloud-free observations. The number of cloud-free observations for the individual pixel of the Sentinel-2 images was recorded in the study areas

(Fig. 2). About 100%, 98.8%, 100%, and 37.1% of pixels had more than 50 cloud-free observations in regions of the Northwest and East coast of England, Chongming Island, and Sansha Bay, respectively. The number of cloud-free observations in Sansha Bay was considerably low compared with other study areas due to the high frequency of cloud cover; however, the minimum number of cloud-free observations still

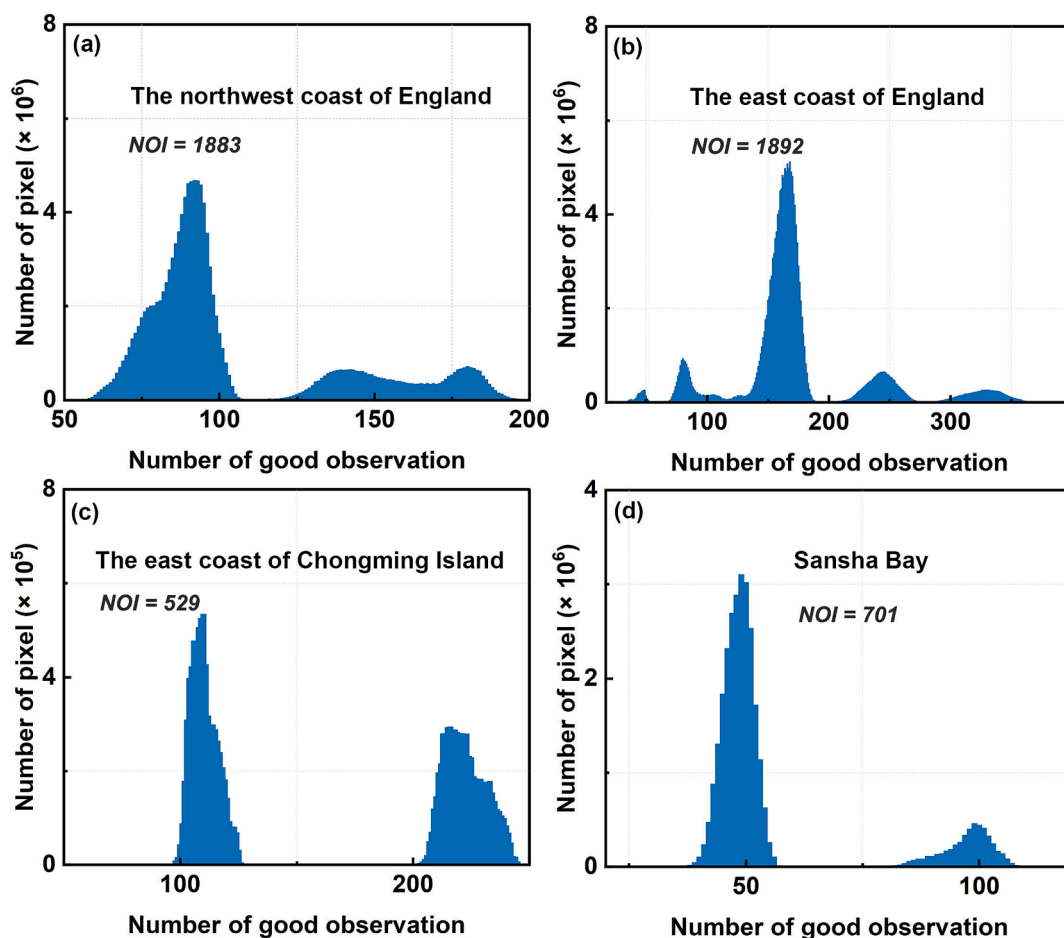


Fig. 2. Histogram of the number of cloud-free Sentinel-2 observations and the number of images used (NOI) in (a) the northwest coast of England, (b) the east coast of England, (c) the east coast of Chongming Island, and (d) Sansha Bay.

reached 36. The acquisition of the Sentinel-2 images and all pre-processing steps were performed on the GEE platform.

2.3. LiDAR and UAV photogrammetric data

We used the available LiDAR data and UAV photogrammetric data in the study areas to establish the relationship between intertidal inundation frequency and the corresponding elevation and to validate our proposed Tide2Topo method. For study areas in England, LiDAR data were captured by the Environment Agency (EA) from March 2020 to April 2021 at the lowest tide and accessed via the Digimap data service platform (<https://digimap.edina.ac.uk>). The data quality was analyzed by EA, which showed that all LiDAR data had good vertical accuracy with a root mean square error (RMSE) of 10 cm, and the spatial resolution varied from 25 cm to 2 m. All LiDAR point clouds were converted into DEMs using the coordinate system of OSGB36 British National Grid. For the study areas in China, 10 UAV photogrammetric surveys were conducted using a DJI Phantom-4 RTK quadcopter with a precise imaging system involving an RTK receiver module in May and October 2021. All UAV flights were conducted during the lowest tide periods at an altitude of 100 m with 80% frontal overlap and 80% side overlap. The UAV images were processed using the SfM photogrammetry algorithm implemented by the Pix4Dmapper software to generate DEMs with the EGM96 vertical datum. The accuracy assessment performed previously showed that the RMSE of UAV photogrammetry could reach up to 5.7 cm with a spatial resolution of 2.7 cm (Chen et al., 2022a). Although sufficient amount of ground data was collected, only one profile in LiDAR-based or UAV photogrammetric DEMs was employed to establish

the relationship between intertidal inundation frequency and elevation for each estuary or bay and the remaining were left for validation. These calibration profiles are depicted in Fig. 1.

3. Methods

Our proposed Tide2Topo is based on a monotonically decreasing relationship between tidal inundation frequency and the corresponding surface elevation. Tidal platforms with higher surface elevations tend to experience a lower frequency and shorter duration of inundation by tides. Therefore, the tidal inundation frequency is considered a geographically relevant indicator of intertidal topographic relief. The general workflow of Tide2Topo intertidal topography mapping is shown in Fig. 3. Specifically, we first combined the water index with the vegetation index to generate water occurrence maps from cloud-free Sentinel-2 time-series. Next, the relationship between inundation frequency and intertidal elevation was modeled by linear and polynomial regression analysis using limited LiDAR or UAV photogrammetric data, which subsequently allowed the construction of large-scale intertidal topography.

3.1. Intertidal water occurrence composite

Numerous spectral-based water and vegetation indices, such as the Normalized Difference Water Index (NDWI) (McFeeters, 1996), modified Normalized Difference Water Index (MNDWI) (Xu, 2006), and the Automated Water Extraction Index (AWEI) (Feyisa et al., 2014), have been used for water body extraction. However, these indices are

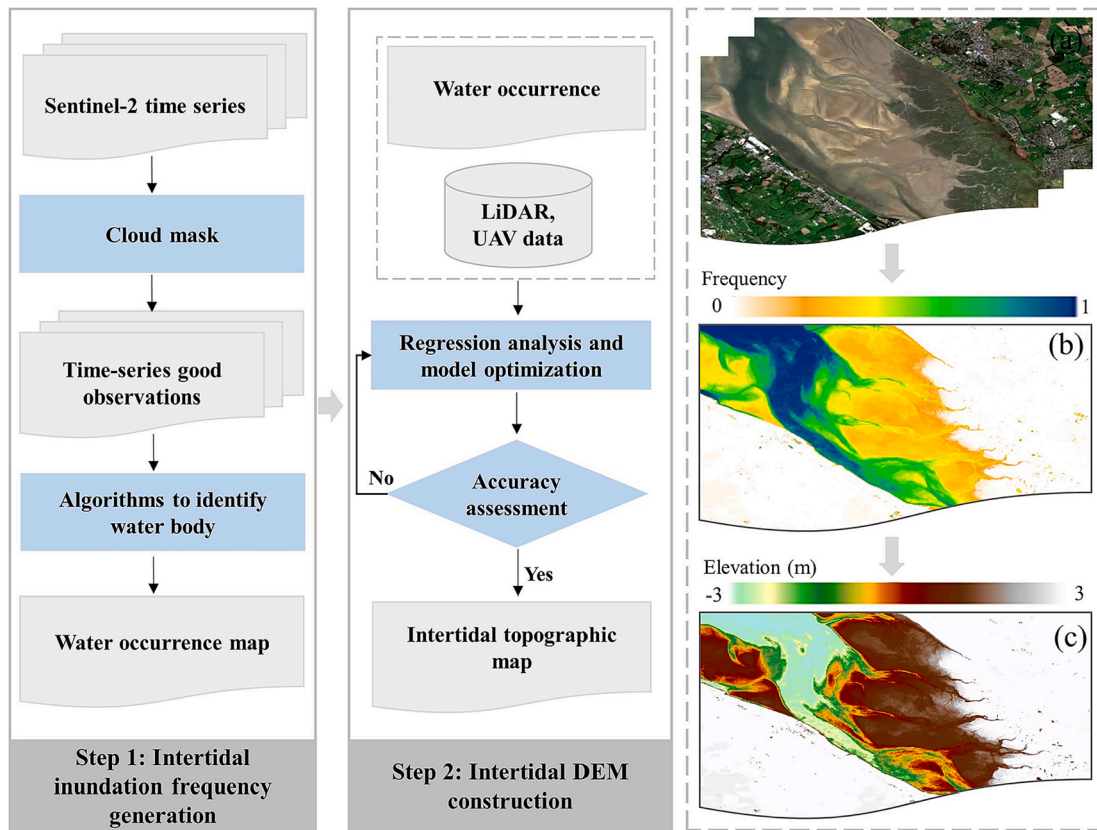


Fig. 3. Workflow of our proposed Tide2Topo intertidal topography mapping and results of key steps: (a) Sentinel-2 time series. (b) Tidal inundation frequency map. (c) Intertidal topography map.

insensitive to salt marsh vegetation inundated by tides, especially in estuaries or bays. To mitigate these effects, an algorithm combining water and vegetation indices was developed by Zou et al. (2017) and subsequently adopted by (Wang et al., 2018) for mapping annual changes in national-scale tidal flats. In this study, we extended the strategy to a new joint NDWI and the Normalized Difference Vegetation Index (NDVI) (Tucker, 1979) algorithm to identify water bodies and Equation (3) expresses this joint criterion.

$$NDWI = (\rho_{green} - \rho_{nir}) / (\rho_{green} + \rho_{nir}) \quad (1)$$

$$NDVI = (\rho_{nir} - \rho_{red}) / (\rho_{nir} + \rho_{red}) \quad (2)$$

$$Water = \begin{cases} 1, & NDWI > T_{Otsu} \text{ and } NDVI < 0.1 \text{ and } (NDWI > NDVI) \\ 0, & \text{others} \end{cases} \quad (3)$$

where ρ_{green} , ρ_{red} , and ρ_{nir} are green, red, and near-infrared (NIR) bands of Sentinel-2 imagery, respectively. T_{Otsu} is the water/land segmentation threshold calculated by the Otsu algorithm (Otsu, 1979). Compared to the approach proposed by Zou et al. (2017), three new criteria were incorporated to identify water body. First, the bands with 10-m resolution were selected uniformly to derive NDWI and NDVI instead of MNDWI due to the difference in spatial resolution, avoiding the errors introduced by upsampling bands with 20-m resolution. Second, the new criteria of $NDWI > T_{Otsu}$ was added to further specify the range of water body pixels. Third, the criteria of $NDVI < 0.1$ was used to exclude vegetation pixels that were misclassified as water body pixels due to tidal inundation. Once the above criterion had been applied to all images to complete water and land segmentation, the tidal inundation frequency was calculated using Equation (4).

$$F_{water} = n_{water} / N \quad (4)$$

where F_{water} is the tidal inundation frequency ranging from 0 to 1, n_{water} is the number of measurements that are classified as water at the pixel location, and N is the total number of good observations at the pixel location.

3.2. Intertidal elevation estimation model development

The decreasing relationship between intertidal elevation and tidal inundation frequency is evident; however, their exact functional relationship is largely influenced by the local intertidal slope and tidal condition. To model such a relationship accurately, six transects in estuaries or bays of the study areas were selected for analysis. The tidal inundation frequency and elevation of these profiles were extracted from Sentinel-2 derived from water occurrence and LiDAR-based or UAV photogrammetric DEMs, respectively. As shown in Fig. 4, the intertidal inundation frequency and elevation demonstrate a significant negative correlation. The trend between intertidal elevation and $1-Frequency$ was roughly consistent. Such a relationship was fitted using a simple linear model (Eq. (5)). However, the overall consistency showed spatial variability across transects as well as within the same transect. For example, the consistency was better in the Chongming Island and Ribble Estuary than in other estuaries or bays. In a specific bay or estuary, such as the Solway Estuary (Fig. 4(a)) and Thames Estuary (Fig. 4(d)), the rate of elevation declined from land to sea and did not exactly coincide with the rate of $1-Frequency$ decrease. To deal with the spatial variability, a third-order polynomial model (Eq. (6)) was designed to regression fit the relationship between intertidal inundation frequency and elevation. Before regression fitting, the DEMs from LiDAR or UAV photogrammetry were resampled to a spatial resolution that was consistent with the sentinel-2 derived water occurrence, i.e., 10-m, using bilinear interpolation. Next, the corresponding point values were extracted along the transects in the area of overlap between the inundation frequency maps

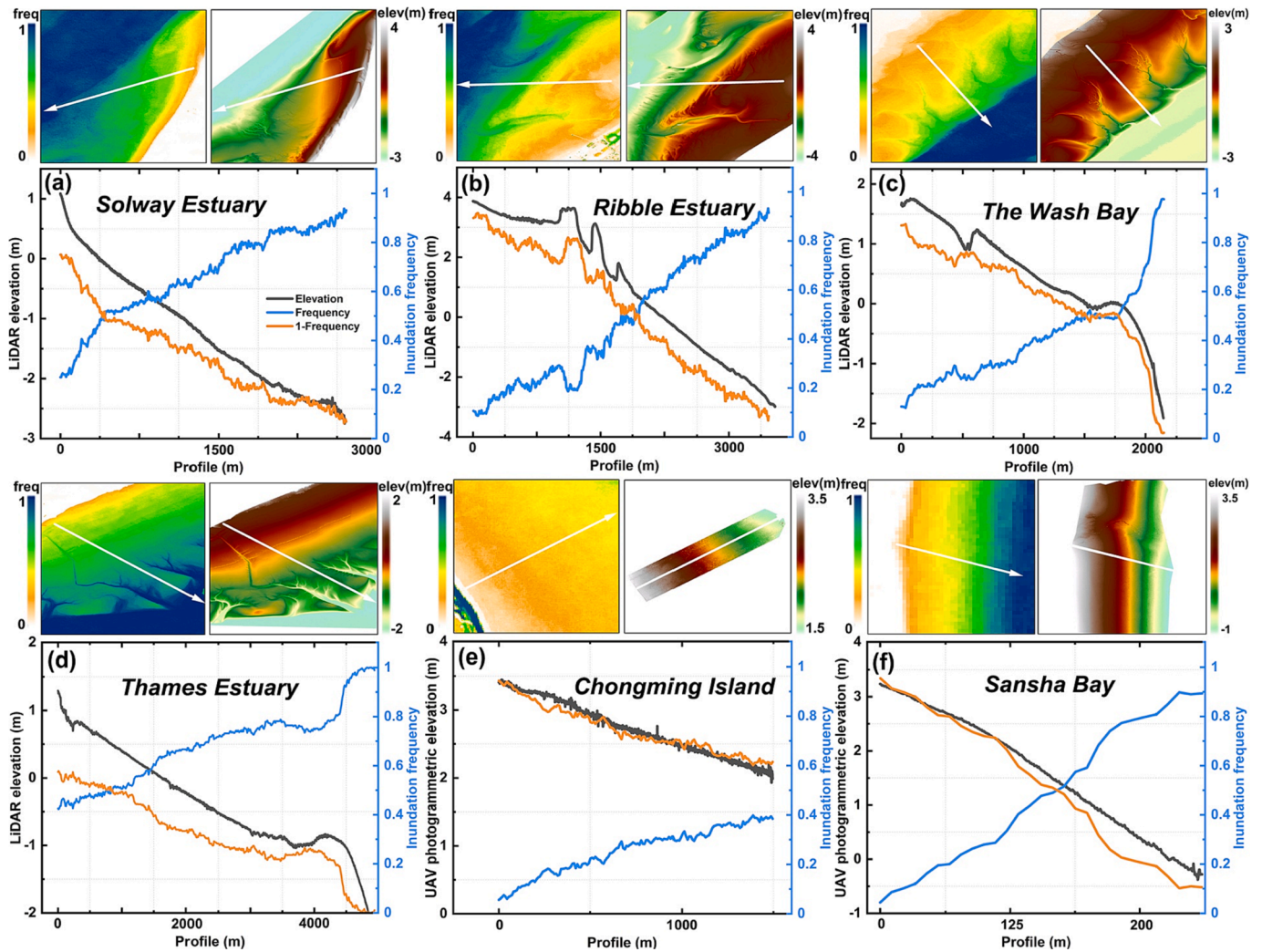


Fig. 4. Analysis of the relationship between intertidal inundation frequency and elevation in six transects of estuaries or bays.

and DEMs to calibrate the linear and polynomial regression models. Once the parameters of regression models were solved, the frequency to elevation mapping transformation was implemented in the GEE platform.

$$H_l = af + b \tag{5}$$

$$H_p = w_0 + w_1f + w_2f^2 + w_3f^3 \tag{6}$$

where H_l and H_p are predicted elevation values for linear and polynomial regression, respectively; f is the inundation frequency derived from Sentinel-2 time series; a , b , w_0 , w_1 , w_2 , w_3 are regression coefficients.

3.3. Accuracy assessment

Validation of intertidal topography mapping includes the following two aspects: (1) validation of water pixel identification during water occurrence composite; and (2) validation of intertidal elevations constructed by two regression models. For the first aspect, because the tide levels in the coastal areas are time-varying, it is challenging to match high-resolution images that are synchronized perfectly with the time of acquisition of Sentinel-2 images. Thus, it is not technically possible to evaluate the accuracy of water extraction at the pixel level as in previous studies (Feyisa et al., 2014; Fisher et al., 2016). Furthermore, the water-land interface is more prone to errors in the extraction of

nearshore water bodies. The semi-open Ribble Estuary and the complex Sansha Bay were considered validation areas, and three images for each area with different tide conditions (i.e., low, middle, and high tide) were selected to quantitatively evaluate the errors. For each image, the water-land boundary was first roughly outlined manually, and next, a 200 m buffer zone was created on both sides of the water-land boundary. Finally, random validation points were generated within the buffer zone (Fig. 5). Each point was visually verified and misclassified points were counted, and subsequently, omission and commission errors were calculated to evaluate the water-land segmentation accuracy. For the second aspect, the LiDAR or UAV photogrammetry DEMs were down-sampled to 10-m and afterward compared to DEMs constructed by the two regression models image-by-image, respectively. Moreover, the accuracy of the constructed intertidal topography was quantitatively assessed using R^2 and the root mean square error (RMSE).

4. Results

4.1. Intertidal water occurrence and accuracy evaluation

Fig. 6 illustrates the spatial extent of unvegetated intertidal zones and the frequency of tidal inundation between January 2020 and December 2021 for the several typical UK and Chinese estuarine coasts or bay shores. The frequency of tidal inundation increased seaward, reflecting the intertidal topographic characteristics in reverse. Low-lying

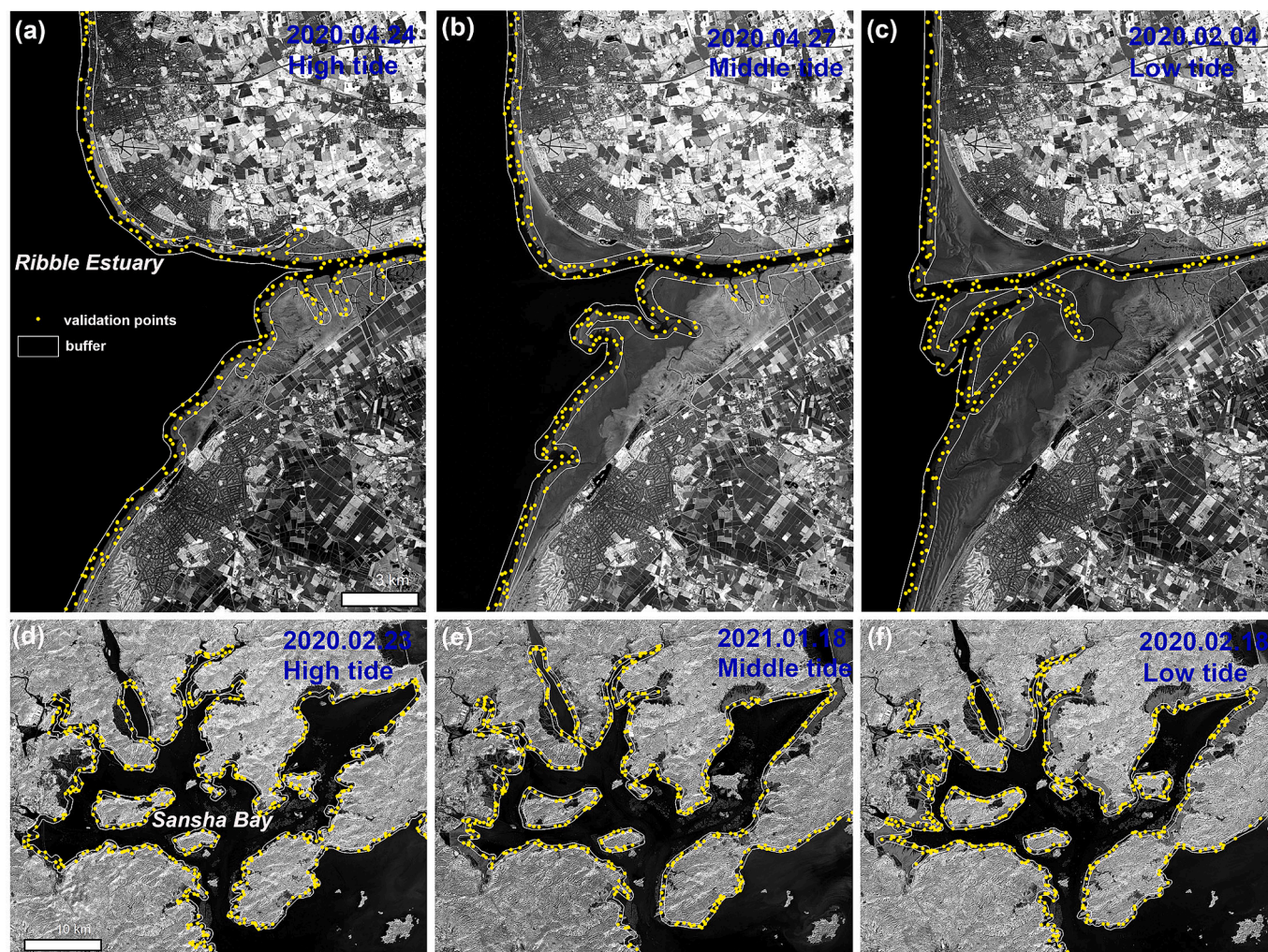


Fig. 5. Spatial distribution of validation points for accuracy assessment of water–land segmentation in (a)–(c) the Ribble Estuary, and (d)–(f) the Sansha Bay under different tide levels.

tidal channels and exposed sandbars in estuaries or bays were evident. For example, the dense networks of tidal channels in Sansha Bay connected to the sea and extended landward. Similarly, tidal channels close to open sea were constantly filled with seawater, and their frequency of inundation approached 100%, whereas those extending landward were subject to periodic tidal inundation and the frequency of inundation gradually decreased until they could not be inundated by the tide (Fig. 6 (f)). These geomorphological features, as reflected in the map of tidal inundation frequency, serve as indicators of intertidal topography.

The results of water–land segmentation accuracy showed that errors of omission and commission at the Ribble Estuary were 1.9% and 0.8%, respectively, whereas they are 1.6% and 1.3%, respectively, in Sansha Bay (Table 1). Accordingly, the average overall accuracy was calculated to be 97.1%. For a convenient inspection, we superimposed water extraction results on the original Sentinel-2 images, and water–land boundaries were highlighted by a conspicuous red color. As illustrated in Fig. 7, our method could distinguish the boundary between water bodies and muddy tidal flats well in Sansha Bay. In addition, it can separate water bodies effectively from sandy shores in the Ribble Estuary. However, minor omission errors of water were present in certain narrow tidal channels at the mouth of the Ribble River (Fig. 7(c)–(d)); however, these were rarely found in tidal channels connected to the sea of the Sansha Bay.

4.2. Intertidal elevation estimation models

For each estuary and bay, the ground observed elevations and the corresponding Sentinel-2-derived tidal inundation frequencies were extracted from a profile line. Next, their relationships were modeled using a simple linear model and a third-order polynomial model, and the results are shown in Fig. 8. Both models achieved good simulation results with small differences, and R^2 ranged from 0.94 to 0.99; however, the polynomial model performed better with a higher R^2 value. In the Solway Estuary, the two modeling functions almost overlapped in the observed frequency range with an identical R^2 value. The simulation differences existed in the high and low-value parts of the tidal inundation frequency in other estuaries or bays, with a few differences in the middle-value part.

4.3. Intertidal elevation mapping and accuracy evaluation

The parameters of simple linear and polynomial models obtained from one profile-based simulation were used for the transformation of inundation frequencies and elevations from local calibration to large scale. The results are shown in Fig. 9, where the topography calculated using the two models was compared with the high-accuracy topography obtained from LiDAR or UAV photogrammetry. The image-by-image visual comparison revealed that both DEMs generated from linear and polynomial models had good consistency with the reference data in

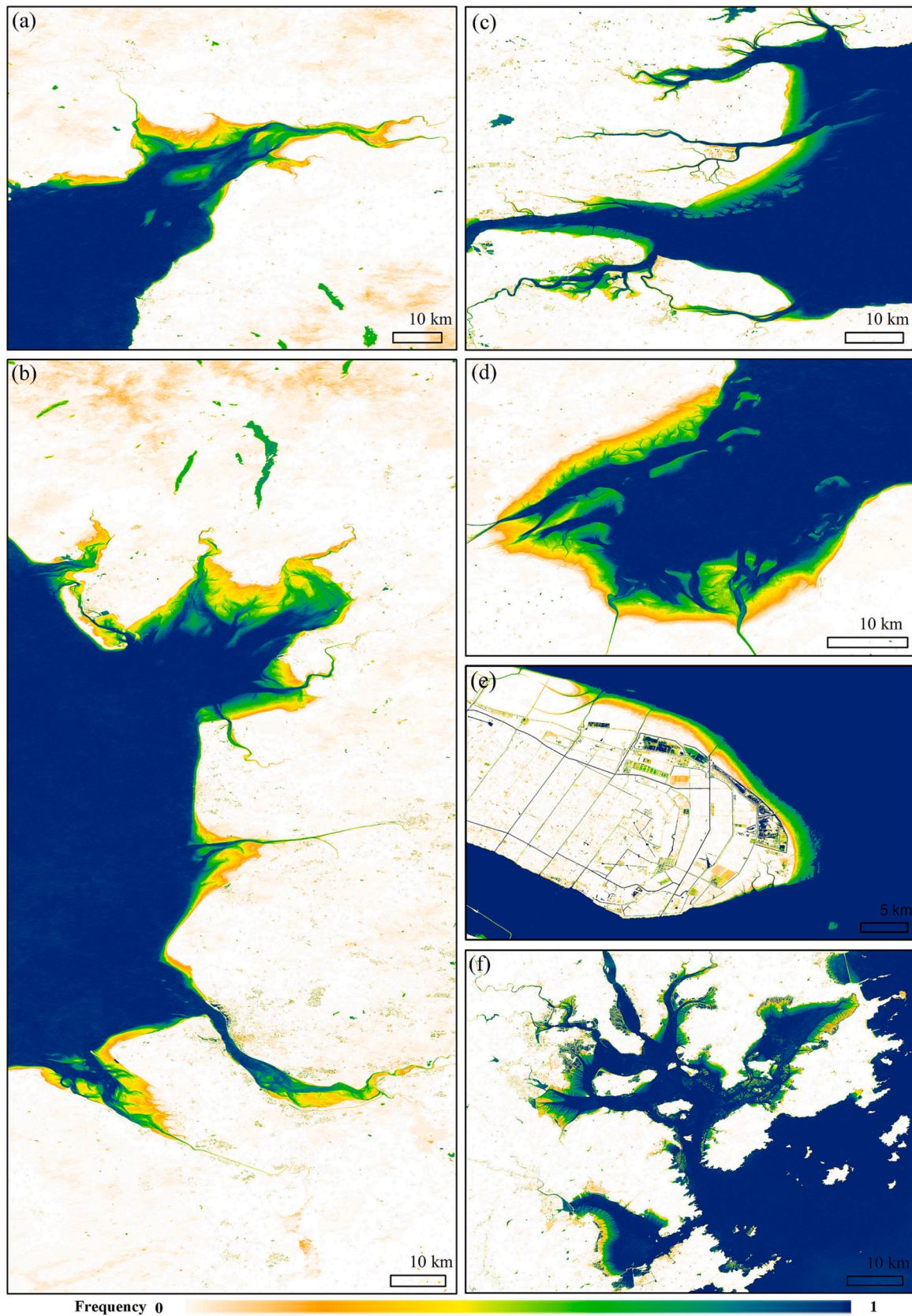


Fig. 6. Maps of water occurrence derived from Sentinel-2 time series in (a) Solway Estuary; (b) Morecambe Bay, Ribble Estuary, and Dee Estuary; (c) Thames Estuary; (d) The Wash Bay; (e) Chongming Island; and (f) Sansha Bay.

Table 1

Accuracy assessment for the water–land segmentation results in Ribble Estuary and Sansha Bay.

Region	Omission error	Commission error	Overall accuracy
Ribble Estuary	1.9%	0.8%	97.2%
Sansha Bay	1.6%	1.3%	97.0%

terms of trend. The results of the point-by-point quantitative evaluation indicated that the accuracy of DEMs constructed by the polynomial model exceeded that of DEMs constructed by the linear model, with a minimum RMSE of 16 cm (Fig. 9(g)) and a maximum RMSE of 38 cm (Fig. 9(h)). Consequently, the calibrated polynomial model was selected to convert the tidal inundation frequencies in the estuaries or bays to the corresponding topography (Fig. 10). These DEMs have a spatial resolution of 10 m and can characterize the general topographic characteristics of intertidal zones well (e.g., elevation gradient, tidal channels, and sandbars).

5. Discussion

5.1. Contributions of Tide2Topo in comparison with previous studies

We developed a novel pixel-based approach, namely Tide2Topo, for constructing large-scale intertidal topography from Sentinel-2 time-series and limited ground truth data. The resulting 10-meter resolution intertidal DEMs in a number of estuaries or bays in the UK and China have been validated with RMSEs ranging from 16 cm to 38 cm. The proposed Tide2Topo method yielded topographic accuracy that was significantly superior to those previously generated using the waterline method (Bishop-Taylor et al., 2019; Sagar et al., 2017; Wang et al., 2019). Similar to the commonly used waterline method, Tide2Topo utilizes tidal amplitudes at different moments to estimate intertidal elevations. However, Tide2Topo avoids the manual selection of images at different tidal levels and instead uses full time-series satellite observations. This ensures finer sampling of the tidal cycle, thereby preventing errors caused by spatial interpolation. In particular, the waterline method tends to extract only the outermost boundary with the sea, ignoring low-lying areas within the intertidal zone, and therefore causes an overestimation of the elevation in these areas when interpolating waterlines. The use of intertidal inundation frequency in Tide2Topo not

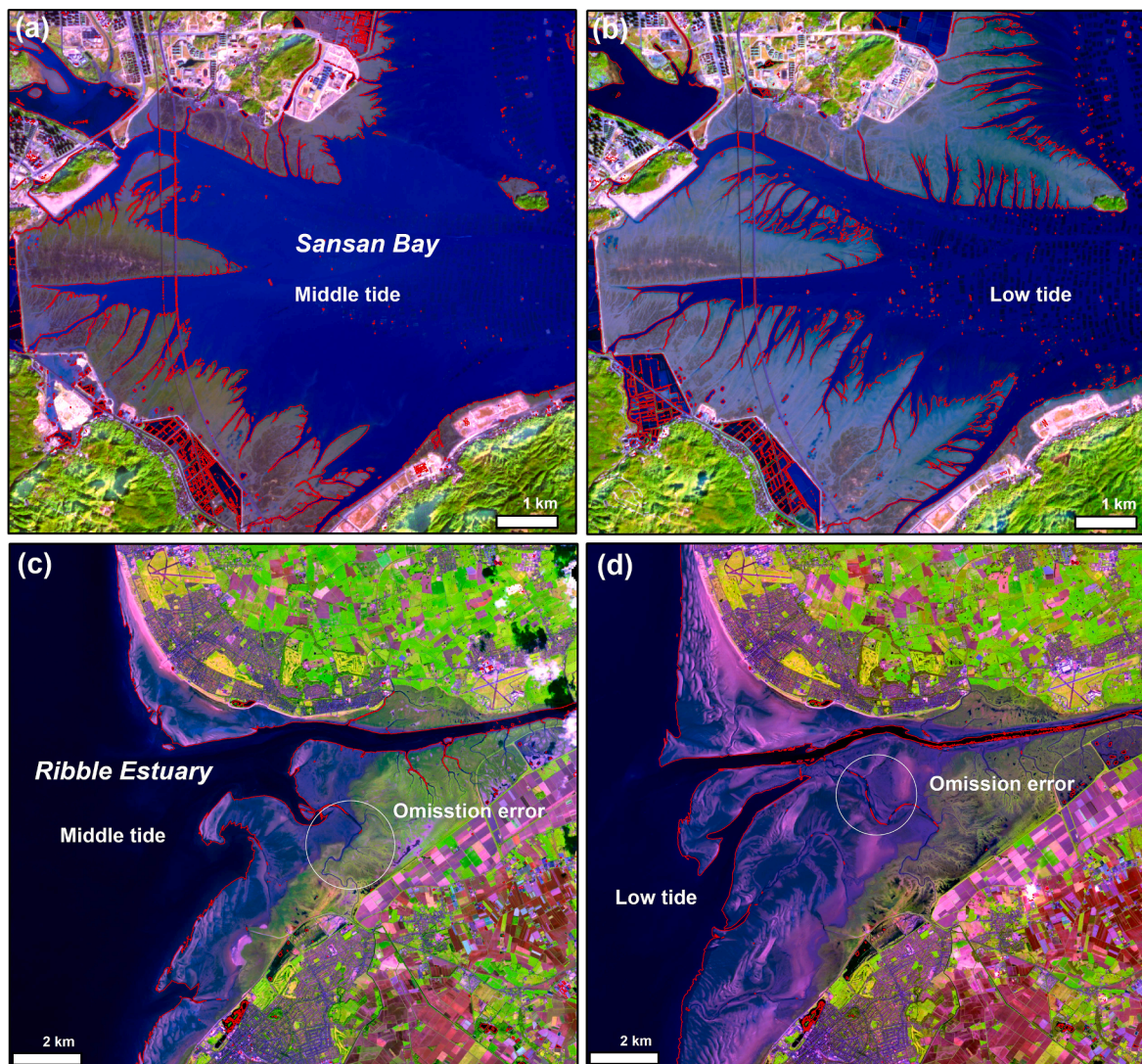


Fig. 7. Visual assessment of water-land segmentation results under different tide conditions: (a)-(b) the Sansha Bay and (c)-(d) Ribble Estuary. The red lines are the water and land boundaries extracted by our method; and the white circles indicate water omission errors in narrow tidal channels. (For interpretation of the references to color in this figure legend, the reader is referred to the web version of this article.)

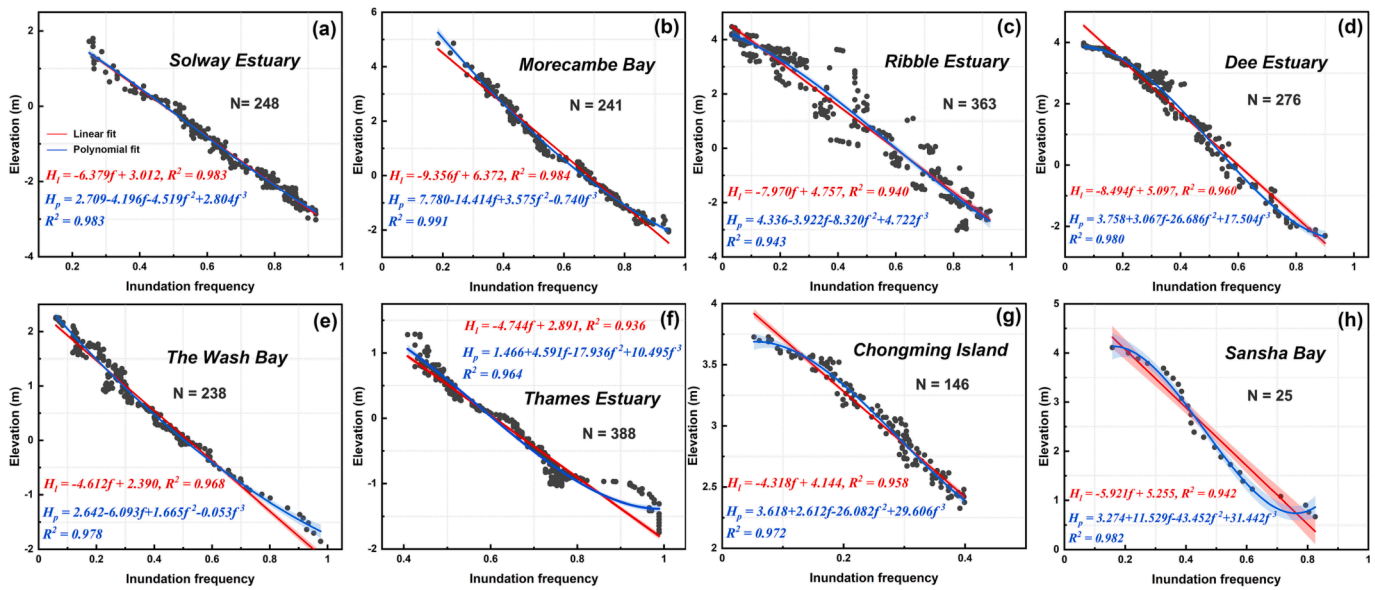


Fig. 8. Analysis of the relationship between intertidal inundation frequency and elevation in six transects of estuaries or bays and the number of records used (N).

only provides pixel-level elevation estimates, but also avoids the labor-intensive process of waterline extraction and the errors arising from waterline delineation offsets (Liu et al., 2013). In addition, Tide2Topo uses ground truth data rather than tide gauge data to calibrate the relationship between pixel-based inundation frequency and elevation based on a polynomial model, thus eliminating the effect on elevation accuracy due to inaccurate tidal data. Note that Tide2Topo only requires a minimal amount of high-accuracy ground measurement data and previous studies have shown that locally high precision, high resolution ground truth observations have been collected in major coastal areas around the world, such as the Yellow River Estuary (Xie et al., 2021), the German Wadden Sea (Benninghoff and Winter, 2019), coasts of Australia (Doyle and Woodroffe, 2018), and Gulf Coast of United States (Johnson et al., 2020). Even in unmapped areas, it is feasible and cost-effective to perform a transect surveying using LiDAR or UAV photogrammetry. Tide2Topo presents an opportunity to complement those fine-scale ground surveys with large-scale satellite observations. Consequently, the data availability, robustness and operational ease of Tide2Topo enable the accurate mapping intertidal elevation at a continental or global scale.

5.2. Impact of the number of available Sentinel-2 data

To extensively cover the full tidal range, Sentinel-2 images from January 2020 to December 2021 with less than 60% cloud cover were selected to calculate the tidal inundation frequency. Tidal flats or sandy beaches morphology inevitably changes over two years; however, tracking associated vertical differences over such a short period is challenging for both satellite-based waterline method and Tide2Topo. Moreover, Tide2Topo aims to construct a large-scale intertidal topography to fill the data gaps in this region and provide key input for medium to long-term coastal dynamic modeling studies. The use of dense Sentinel-2 data provides a finer and more complete coverage of the tidal range than previous studies such as using Landsat archives as the data source (Tseng et al., 2017). Thus, a compromise was achieved between the number of available Sentinel-2 images and rigorous consideration of coastal morphological stability during image acquisition. This trade-off has been indicated as acceptable in previous studies that constructed intertidal DEM using the waterline method based on multi-temporal Landsat images (Mason et al., 2010; Salameh et al., 2020). Furthermore, the intertidal topography of most estuaries or bays does not change dramatically in the short term. High-precision unmanned

photographic surveys, for example, revealed that most mudflat topographic changes in the Yangtze Estuary ranged from 10 cm to 20 cm per year (Chen et al., 2022b). For changes of this magnitude, the above trade-off is reasonable. However, intertidal topography could change rapidly in short term for some estuaries with high water discharge and sediment load, such as the Amazon estuary (Gensac et al., 2016). When using Tide2Topo to map estuarine intertidal topography, it is necessary to consider the annual variability of the topography and select a reasonable date range for the satellite images.

Nevertheless, because Tide2Topo is a pixel-based method for intertidal topography estimation, we need to study the sensitivity and uncertainty of the number of available Sentinel-2 cloud-free observations. Fig. 11 shows the coverage of the tidal cycle provided by Sentinel-2 for the Thames Estuary in 2020–2021, 2020, and 2021, respectively, as well as the tidal inundation frequencies calculated based on cloud-free observations during the corresponding periods. In the ideal cloud-free scenario, Sentinel-2 acquired 580 observations at a given pixel location in the Thames Estuary between 2020 and 2021. The tidal heights associated with these image acquisition dates almost covered the entire tidal range of the region completely (Fig. 11(b)). The number of good observations remaining after the removal of cloudy pixels was 181, with several breaks in the corresponding tidal coverage; however, the difference in the tidal height between the breaks did not exceed 20 cm. However, if only 1 year of Sentinel-2 images were used, e.g., 2020 or 2021, the number of good observations was halved, and there were more significant breaks in the tidal coverage. Thus, these breaks were presented as stepped changes in the tidal inundation frequency maps, as shown in Fig. 11(g). Accordingly, the resulting estimated intertidal topography exhibited a discontinuous variation. Although these discontinuities can be resolved using spatial interpolation as in the waterline method, the resulting DEMs are substantially less representative of the actual surface elevation.

5.3. Effect of water body extraction errors on results

The number of times a pixel is marked for water within a given time-series determines the value of the tidal inundation frequency, and misclassification of that pixel as water or land overestimates or underestimates the inundation frequency and, accordingly, an underestimation or overestimation of the associated elevation. To quantify the effect of water body misclassification on the generated topography at the pixel scale, we calculated the elevation errors arising from the

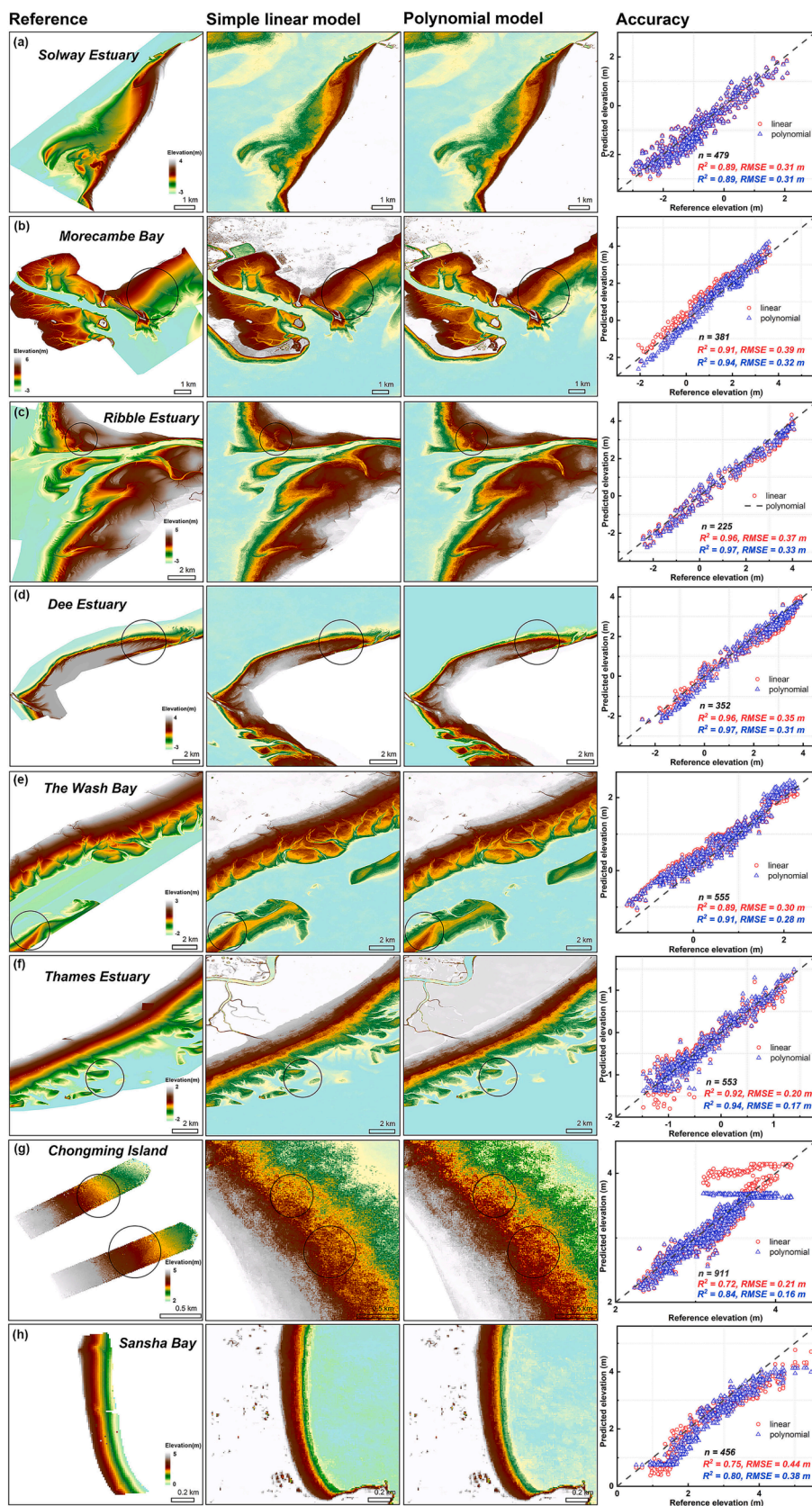


Fig. 9. Comparison of elevation estimation results from different models and their accuracy evaluation.

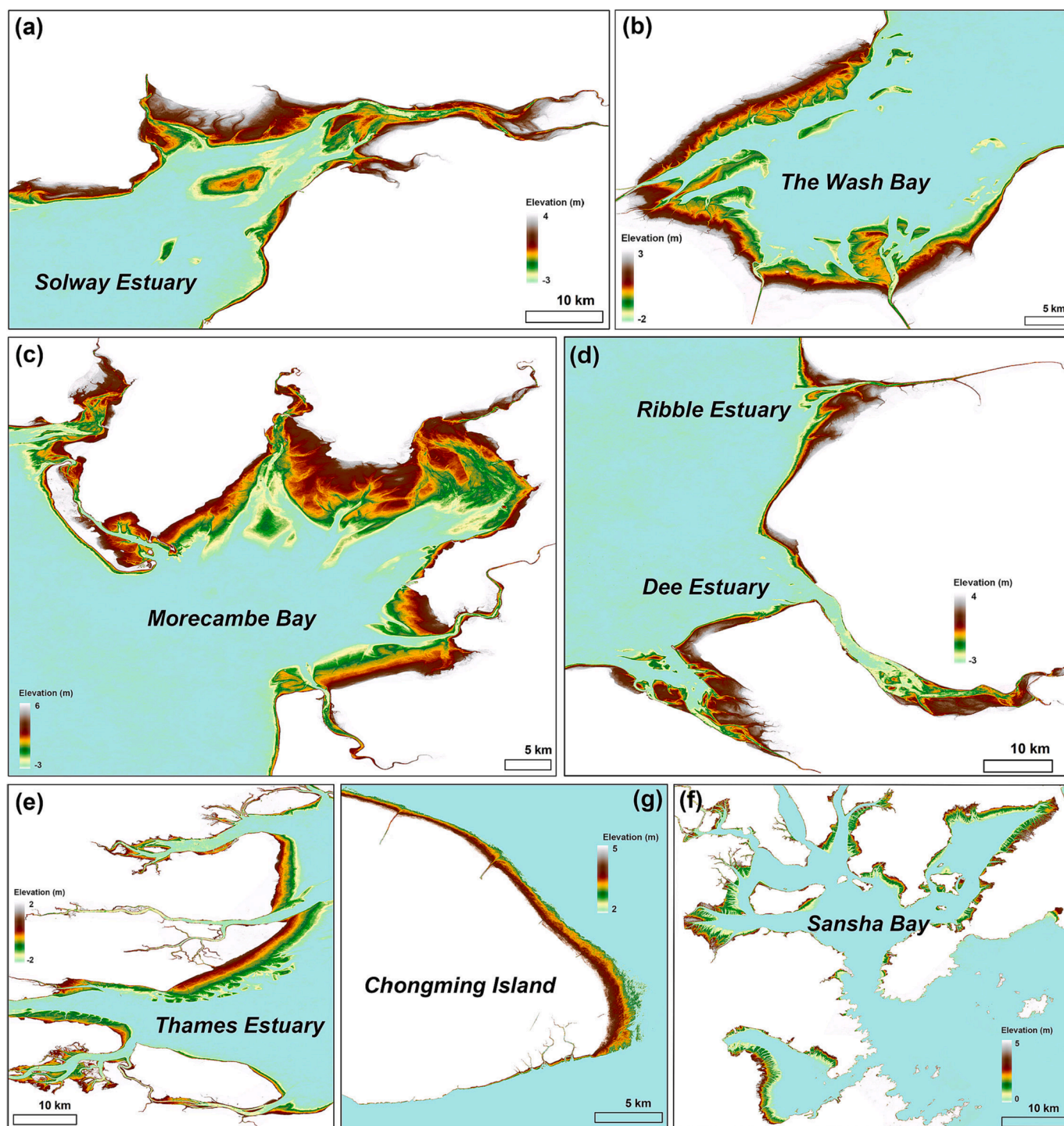


Fig. 10. Intertidal topography transformed from tidal inundation frequency using polynomial models.

cumulative number of misclassifications for different inundation frequencies. For example, in the Thames Estuary, the true tidal inundation frequency of a pixel was 0.1, and the number of misclassifications in practice was assumed to range from 1 to 10, and the resulting corresponding elevation errors were subsequently calculated. The results demonstrated that for a given pixel, the resulting elevation error increased with the cumulative number of misclassifications at that pixel location in the image collection used (Fig. 12(a)). Because the third-order polynomial model is non-linear, the same cumulative misclassification error resulted in different elevation errors for different true tidal inundation frequencies. The resulting elevation errors were larger for

the true tidal inundation frequencies between 0.4 and 0.7, and an accumulated misclassification of more than seven times resulted in elevation differences of more than 20 cm. Fortunately, the overall accuracy of about 97% for the water-land segmentation implied that the number of misclassifications was limited, ensuring the controllability and reliability of the proposed Tide2Topo. Furthermore, the accuracy assessment revealed that these misclassification errors occurred primarily in areas near the tidal channels (Fig. 7). This misclassification could result from one of the three factors: 1) tidal channels are pathways for the exchange of water and sediment during ebb and flood, and the rapid changes in water level within them might be out of sync with tidal

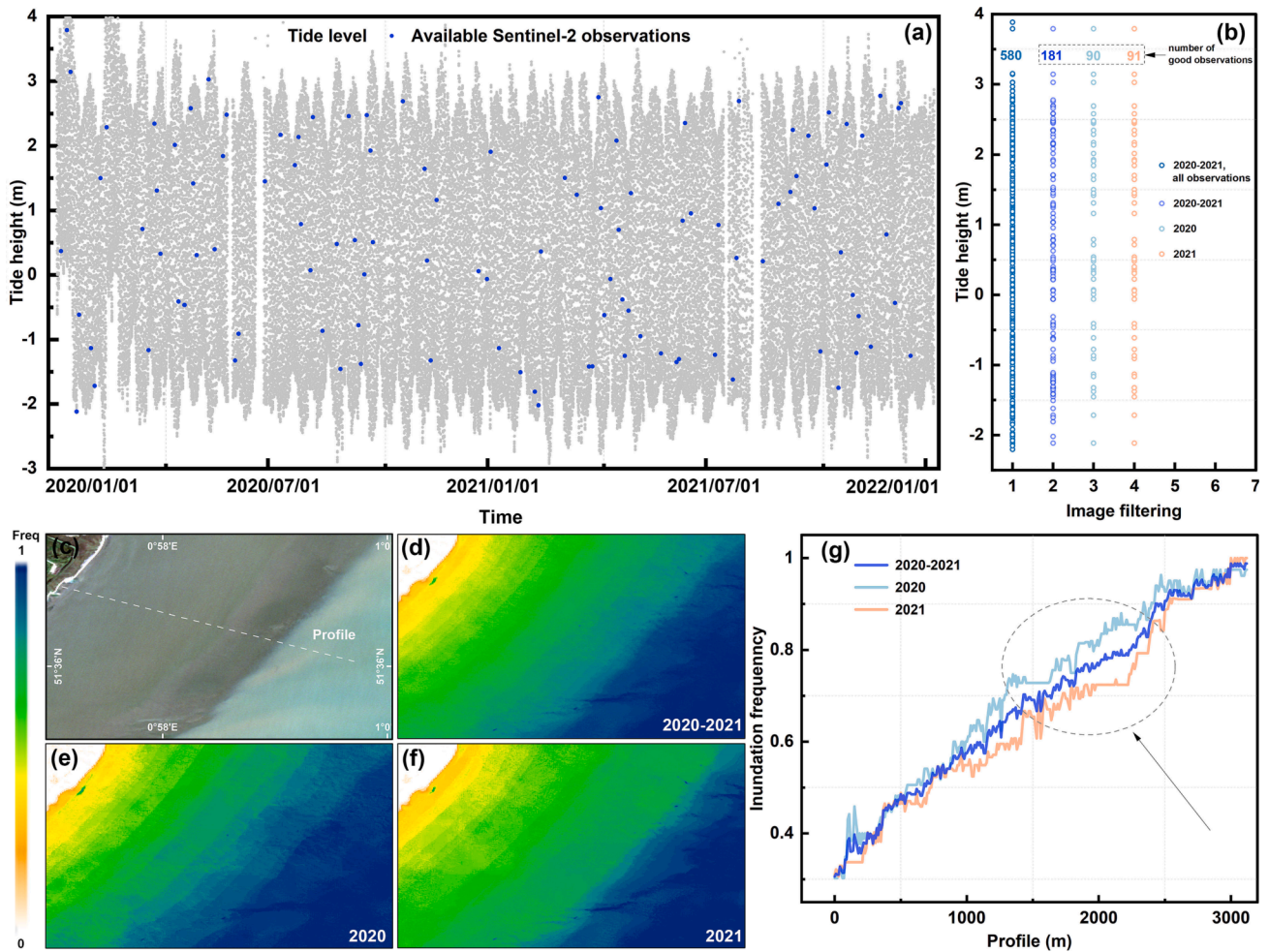


Fig. 11. (a) The plots of the tidal coverage provided by Sentinel-2 images used for the Thames Estuary in 2020–2021. (b) Collection of tidal heights at the acquisition moment of Sentinel-2 for different scenarios. (c)–(f) Tidal inundation frequency maps. (g) Comparison of one profile morphology in these maps.

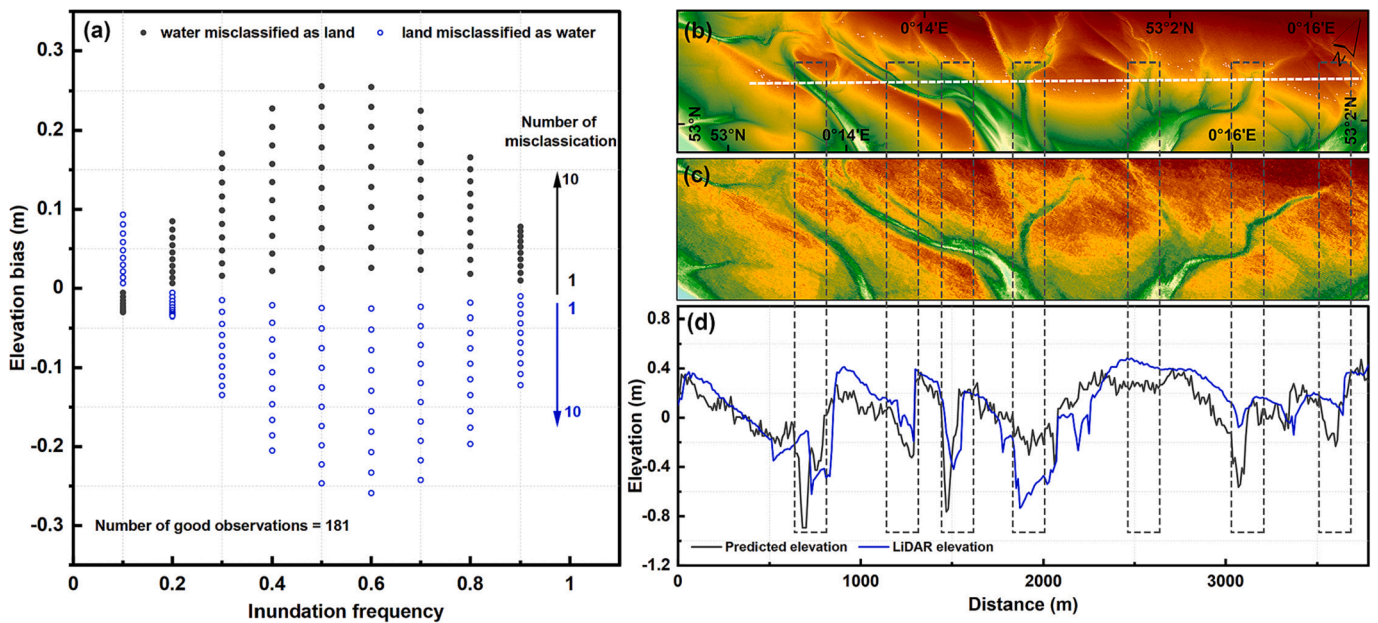


Fig. 12. (a) Elevation bias caused by misclassification errors of water bodies under different true tidal inundation frequency cases. (b) LiDAR-based DEM. (c) Constructed DEM. (d) Comparison of profile morphology in two DEMs.

inundation in the tidal flats; 2) the water in tidal channels is extremely turbid, and the NIR band of the NDWI index used is sensitive to high suspended sediment concentrations and prone to misclassification (Guo et al., 2017). Although the shortwave infrared radiation (SWIR) band of the MNDWI index can handle with highly turbid water (Jain et al., 2022), the spatial resolution of the SWIR band in Sentinel-2 is 20 m, and upsampling to 10 m could introduce errors; 3) the narrow width of the tidal channels and their high proportion of mixed pixels in Sentinel-2 imagery. Accordingly, comparison of the constructed DEM (Fig. 12(c)) with the LiDAR-based DEM (Fig. 12(b)) revealed that the elevation differences around the tidal channels were significantly larger than those in other regions, up to 40 cm, which is consistent with the theoretical assessment above. In comparison to LiDAR-based DEMs in other areas excluding tidal channels, Tide2Topo can create intertidal topography with elevation errors as low as 10 cm.

5.4. Selection of representative ground truth surveys used for calibration

The accuracy of the waterline method was restricted by the accuracy of the simulated or measured tidal levels used to calibrate the waterline elevation (Gao et al., 2021; Sagar et al., 2017). The Tide2Topo utilized high-precision elevations and the corresponding tidal inundation frequencies extracted from one profile morphology to calibrate regression parameters. Hence, the Tide2Topo algorithm also suffers from the selection of ground surveys used for calibration. Representative profiles are required to extend seaward over the intertidal range exposed during low tide to avoid underfitting regression equations in areas where no data are available. In addition, spatial differences exist in the instantaneous tidal field due to phase differences in tidal wave propagation and tidal deformation caused by the complexity of underwater topography. For example, the tidal gauge stations at Workington, Heysham, and Liverpool are spatially separated by more than 50 km, whereas the difference in the tidal height at the same moment varies by up to half a meter (Fig. 13(b)). Thus, the assumption that intertidal areas with the same tidal inundation frequency have the same elevation holds only on a limited spatial range, implying that the regression relationship established by a profile at a given location can only be mapped to a limited spatial extent theoretically.

To explore the spatial extent that can be controlled by one calibration profile, three DEMs were constructed using one profile located in the Solway Estuary, Morecambe Bay, and Ribble Estuary. Five transects with direct distances from 1 km to 160 km from the calibration profiles were used for validation. As shown in Fig. 13, the DEMs constructed based on the Solway transect, the Morecambe transect, or the Ribble transect showed a similar pattern in topographic accuracy compared with the LiDAR-based DEM: their degree of closeness to the calibration transect was related to higher topographic accuracy of the evaluation transect. In this case, the accuracy of the constructed topography remained high with an RMSE of approximately 40 cm within 50 km from the calibration profiles; however, it decreased significantly to around 70 cm when the distance reached 80 km and to roughly 80 cm when the distance exceeded 100 km. Therefore, Tide2Topo has a limited requirement for ground truth surveys in intertidal topographic mapping, enabling it to be employed in national or global topographic mapping. The above evaluation provides practicable guidelines for the location and number of representative profiles to be collected for intertidal mapping at the national or global scale.

Furthermore, while the calibration data used in this paper were obtained at the lowest tide, it is worth discussing the calibration model selection, and the implications for the results of the calibration data are insufficient to cover the seaward width of the intertidal zone. Using Morecambe Bay as an example, the LiDAR data within 1 km of the seaward side were manually removed to simulate the calibration data being acquired at the non-lowest tide (Fig. 14). To fit the elevation measured at the non-lowest tide and the corresponding tidal inundation frequency, a linear model and a polynomial were used, respectively. The

polynomial model was found to be locally optimal over the intertidal width covered by the calibration data (i.e., within the range of the corresponding tidal inundation frequency) but underperformed everywhere else. Conversely, the linear model fits well over the range of tidal inundation frequency not covered by the calibration data because its slope is constant and in good agreement with the intertidal topographic gradient. When using Tide2Topo for intertidal topographic mapping, choosing the linear model for elevation calibration will help to avoid large errors if the calibration data do not cover the entire range of tidal inundation frequency.

5.5. Future works

The construction of pixel-based intertidal topography using the Tide2Topo requires dense satellite observations sufficient to cover the complete tidal range. Although the revisit period of the Sentinel-2 twin-satellite constellation is considerably short, the high-frequency cloud coverage in the coastal areas considerably reduces the available images. As an advanced radar mission, Sentinel-1 mission can deliver images day and night under all weather conditions. In addition, it can provide numerous available images and obtain a complete sampling of the tidal range for a short period. However, extracting exposed muddy flats or sandy beaches with Sentinel-1 SAR data remains challenging. For instance, there is a large overlap in the radar backscattering distribution between wet tidal flats, general tidal flats, and water bodies, making it difficult for conventional threshold methods to accurately separate exposed tidal flats from water bodies (Fig. 15). Future work in intertidal topography construction with Sentinel-1 SAR images should focus on developing adaptive or deep learning-based methods to deal with the local complexity and tidally spatial variation of exposed tidal flats. Once the difficulty has been solved, Sentinel-1 data can be applied to the Tide2Topo framework to map large-scale intertidal topography and monitor intertidal geomorphological changes at a seasonal or annual time scale.

6. Conclusions

Intertidal topography is fundamental information for coastal dynamics modeling and coastal wetland restoration. Previous approaches to intertidal topography construction have been restricted by methodological portability and automatization, the spatial coverage of mapping, accuracy, and efficiency, thereby limiting their extending potential at the global scale. To solve these problems, we proposed a novel method of Tide2Topo, to accurately construct large-scale intertidal topography with high resolution. Regression analysis was used to establish the relationship between the local tidal inundation frequency derived from the Sentinel-2 time-series and the corresponding elevation from limited ground truth surveys. Next, the obtained parameters were applied to the other tidal inundation frequency to complete the construction of the large-scale intertidal topography. The main conclusions of the study are as follows:

Tidal inundation frequency derived from the full time-series Sentinel-2 can well characterize intertidal topography. Compared with the linear model, the third-order polynomial model can better represent its relationship with the surface elevation.

The intertidal topography constructed by the proposed Tide2Topo method has high accuracy. Compared to the commonly used waterline method, the Tide2Topo method does not require manual image selection and additional modifications of the waterline. Therefore, it is simple to implement and readily generalizable to continental or global scale.

The performance of the Tide2Topo is subject to the number of satellite observations, and adequate observations are required to ensure complete sampling of the full tidal range. The effect of the bias of the computed tidal inundation frequency caused by water extraction errors on Tide2Topo can be evaluated quantitatively and has been demonstrated to be bounded and moderate.

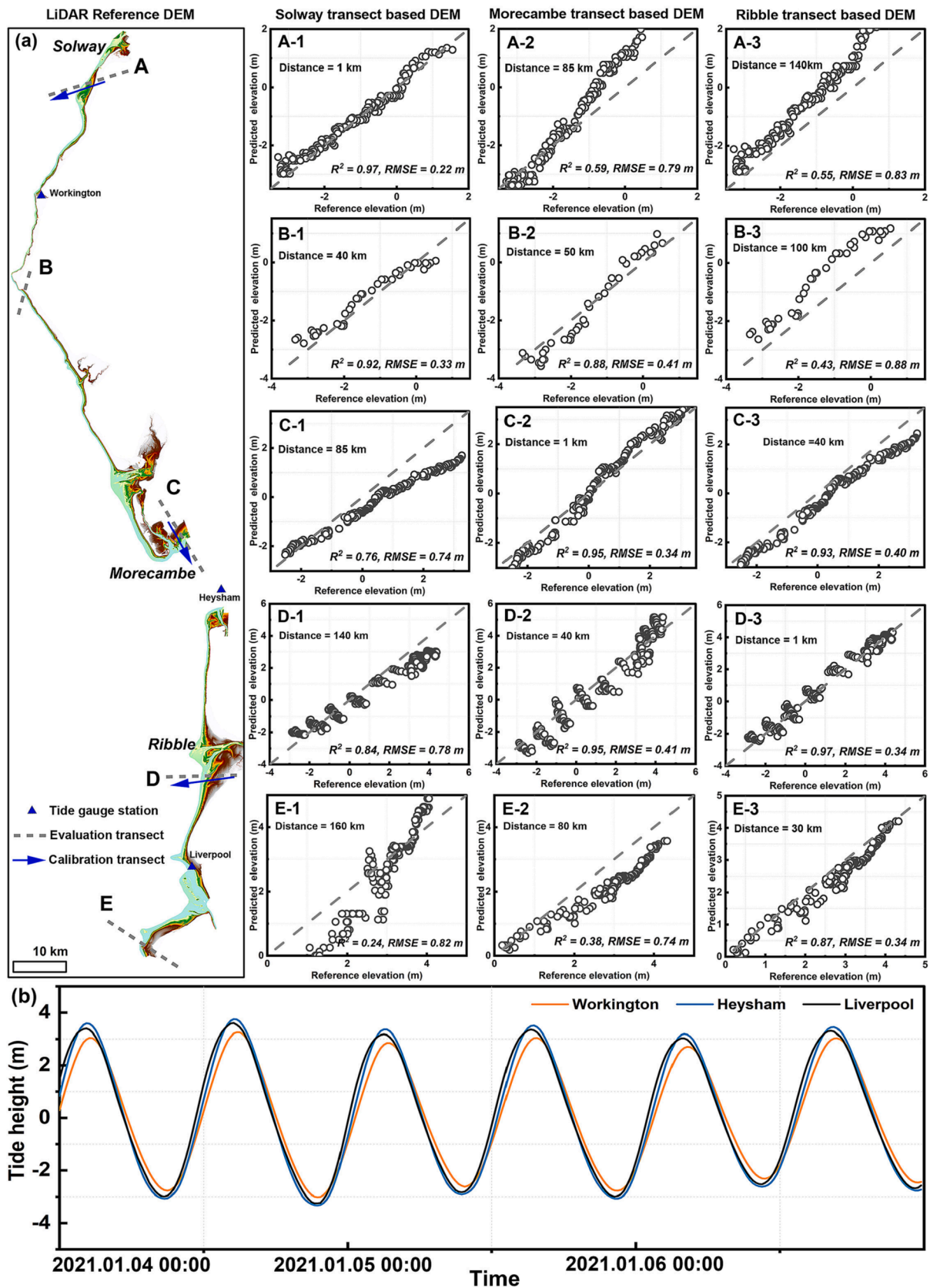


Fig. 13. (a) Exploration of the control range of calibration profiles in the Solway Estuary, Morecambe Bay, and Ribble Estuary. (b) The differences in tide height at the same moment in the tide gauge stations at Workington, Heysham, and Liverpool.

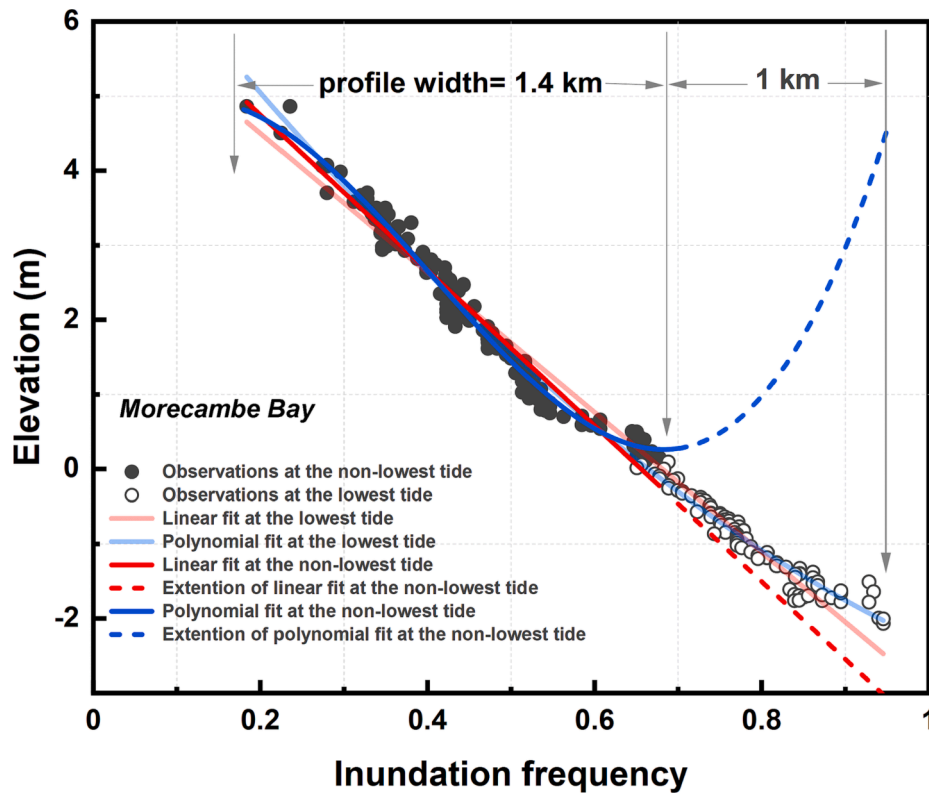


Fig. 14. Simulation of the effect using calibration data collected at the non-lowest tide.

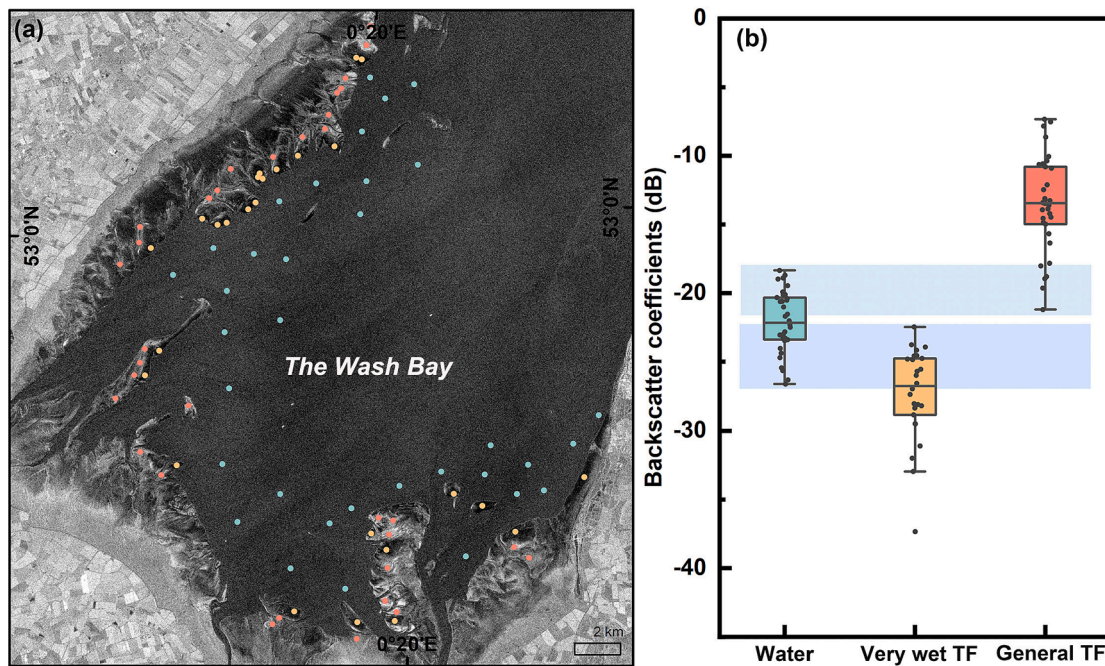


Fig. 15. Distribution of SAR backscatter coefficients (VH polarization) from Sentinel-1 for water, very wet tidal flats, and general tidal flats in the Wash Bay.

In addition, Tide2Topo is agnostic to sensors and platform. Our future work will incorporate Sentinel-1 SAR as data source, with images day and night under all weather conditions to capture complete sampling of the full tide range in a short period, such that we can monitor intertidal topography at a seasonal or annual time scale.

Declaration of Competing Interest

The authors declare that they have no known competing financial interests or personal relationships that could have appeared to influence the work reported in this paper.

Acknowledgments

This work was supported by the Natural Environment Research Council [grant number NE/T004002/1]. The research was partially funded by the project “Coping with Deltas in Transition” within the Programme of Strategic Scientific Alliances between China and the Netherlands (PSA), financed by the Ministry of Science and Technology of the People’s Republic of China (MOST) [grant number 2016YFE0133700], and also sponsored by the China Scholarship Council (CSC).

References

- Andrioli, U., Almeida, L.P., Almar, R., 2018. Coupling terrestrial LiDAR and video imagery to perform 3D intertidal beach topography. *Coast Eng.* 140, 232–239.
- Bell, P.S., Bird, C.O., Plater, A.J., 2016. A temporal waterline approach to mapping intertidal areas using X-band marine radar. *Coast Eng.* 107, 84–101.
- Benninghoff, M., Winter, C., 2019. Recent morphologic evolution of the German Wadden Sea. *Sci. Rep.* 9 (1), 1–9.
- Bergsma, E.W., Almar, R., Rolland, A., Binet, R., Brodie, K.L., Bak, A.S., 2021. Coastal morphology from space: a showcase of monitoring the topography-bathymetry continuum. *Remote Sens. Environ.* 261, 112469.
- Bertels, L., Houthuys, R., Sterckx, S., Knaeps, E., Deronde, B., 2011. Large-scale mapping of the riverbanks, mud flats and salt marshes of the Scheldt basin, using airborne imaging spectroscopy and LiDAR. *Int. J. Remote Sens.* 32 (10), 2905–2918.
- Bishop-Taylor, R., Sagar, S., Lymburner, L., Beam, R.J., 2019. Between the tides: modelling the elevation of Australia’s exposed intertidal zone at continental scale. *Estuar Coast Shelf S* 223, 115–128.
- Bishop-Taylor, R., Nanson, R., Sagar, S., Lymburner, L., 2021. Mapping Australia’s dynamic coastline at mean sea level using three decades of Landsat imagery. *Remote Sens. Environ.* 267, 112734.
- Brunier, G., Michaud, E., Fleury, J., Anthony, E.J., Morvan, S., Gardel, A., 2020. Assessing the relationship between macro-faunal burrowing activity and mudflat geomorphology from UAV-based structure-from-motion photogrammetry. *Remote Sens. Environ.* 241, 111717.
- Cao, W., Zhou, Y., Li, R., Li, X., 2020. Mapping changes in coastlines and tidal flats in developing islands using the full time series of Landsat images. *Remote Sens. Environ.* 239.
- Chen, C., Zhang, C., Schwarz, C., Tian, B., Jiang, W., Wu, W., Garg, R., Garg, P., Aleksandr, C., Mikhail, S., 2022a. Mapping three-dimensional morphological characteristics of tidal salt-marsh channels using UAV structure-from-motion photogrammetry. *Geomorphology* 407, 108235.
- Chen, C., Zhang, C., Wu, W., Jiang, W., Tian, B., Zhou, Y., 2022b. Application of UAV-based photogrammetry without ground control points in quantifying intertidal mudflat morphodynamics, IGARSS 2022–2022 IEEE international geoscience and remote sensing symposium. *IEEE* 7767–7770.
- Coluzzi, R., Imbrenda, V., Lanfredi, M., Simonello, T., 2018. A first assessment of the Sentinel-2 Level 1-C cloud mask product to support informed surface analyses. *Remote Sens. Environ.* 217, 426–443.
- Doyle, T.B., Woodroffe, C.D., 2018. The application of LiDAR to investigate foredune morphology and vegetation. *Geomorphology* 303, 106–121.
- Feyisa, G.L., Meilby, H., Fensholt, R., Proud, S.R., 2014. Automated water extraction index: a new technique for surface water mapping using landsat imagery. *Remote Sens Environ* 140, 23–35.
- Fisher, A., Flood, N., Danaher, T., 2016. Comparing Landsat water index methods for automated water classification in eastern Australia. *Remote Sens. Environ.* 175, 167–182.
- Gao, W., Shen, F., Tan, K., Zhang, W., Liu, Q., Lam, N.S., Ge, J., 2021. Monitoring terrain elevation of intertidal wetlands by utilising the spatial-temporal fusion of multi-source satellite data: a case study in the Yangtze (Changjiang) Estuary. *Geomorphology* 383, 107683.
- Gensac, E., Martinez, J.-M., Vantrepotte, V., Anthony, E.J., 2016. Seasonal and inter-annual dynamics of suspended sediment at the mouth of the Amazon river: the role of continental and oceanic forcing, and implications for coastal geomorphology and mud bank formation. *Cont. Shelf Res.* 118, 49–62.
- Guo, Q., Pu, R., Li, J., Cheng, J., 2017. A weighted normalized difference water index for water extraction using Landsat imagery. *Int. J. Remote Sens.* 38 (19), 5430–5445.
- Heygster, G., Dannenberg, J., Notholt, J., 2010. Topographic mapping of the german tidal flats analyzing SAR images with the waterline method. *IEEE Trans. Geosci. Remote Sens.* 48 (3), 1019–1030.
- Hill, N.K., Woodworth, B.K., Phinn, S.R., Murray, N.J., Fuller, R.A., 2021. Global protected-area coverage and human pressure on tidal flats. *Conserv. Biol.* 35 (3), 933–943.
- Huff, T.P., Feagin, R.A., Delgado, A., 2019. Understanding lateral marsh edge erosion with terrestrial laser scanning (TLS). *Remote Sens.* 11 (19), 2208.
- Jain, A., Ramakrishnan, R., Thomaskutty, A., Agrawal, R., Rajawat, A., Solanki, H., 2022. Topography and morphodynamic study of intertidal mudflats along the eastern coast of the Gulf of Khambhat, India using remote sensing techniques. *Remote Sens. Appl.: Soc. Environ.* 27, 100798.
- Jia, M.M., Wang, Z.M., Mao, D.H., Ren, C.Y., Wang, C., Wang, Y.Q., 2021. Rapid, robust, and automated mapping of tidal flats in China using time series Sentinel-2 images and Google Earth Engine. *Remote Sens. Environ.* 255.
- Johnson, C.L., Chen, Q., Ozdemir, C.E., 2020. Lidar time-series analysis of a rapidly transgressing low-lying mainland barrier (Caminada Headlands, Louisiana, USA). *Geomorphology* 352, 106979.
- Kulp, S.A., Strauss, B.H., 2018. CoastalDEM: a global coastal digital elevation model improved from SRTM using a neural network. *Remote Sens. Environ.* 206, 231–239.
- Lee, S.-K., Ryu, J.-H., 2017. High-accuracy tidal flat digital elevation model construction using TanDEM-X science phase data. *IEEE J. Sel. Topics Appl. Earth Observ. Remote Sens.* 10 (6), 2713–2724.
- Li, H., Cutler, M., Zhang, D., Daramola, S., Zhu, Y., Gong, Z., 2022. Retrieval of tidal flat elevation based on remotely sensed moisture approach. *IEEE J. Sel. Topics Appl. Earth Observ. Remote Sens.* 15, 5357–5370.
- Li, Z., Heygster, G., Notholt, J., 2014. Intertidal Topographic Maps and Morphological Changes in the German Wadden Sea between 1996–1999 and 2006–2009 from the Waterline Method and SAR Images. *IEEE J. Sel. Topics Appl. Earth Observ. Remote Sens.* 7 (8), 3210–3224.
- Liu, Y., Huang, H., Qiu, Z., Fan, J., 2013. Detecting coastline change from satellite images based on beach slope estimation in a tidal flat. *Int. J. Appl. Earth Obs.* 23, 165–176.
- Loke, L.H., Todd, P.A., 2016. Structural complexity and component type increase intertidal biodiversity independently of area. *Ecology* 97 (2), 383–393.
- Mason, D., Davenport, I., Robinson, G., Flather, R., McCartney, B., 1995. Construction of an inter-tidal digital elevation model by the ‘Water-Line’ Method. *Geophys. Res. Lett.* 22 (23), 3187–3190.
- Mason, D.C., Davenport, I.J., Flather, R.A., Gurney, C., Robinson, G.J., Smith, J.A., 2001. A sensitivity analysis of the waterline method of constructing a digital elevation model for intertidal areas in ERS SAR scene of Eastern England. *Estuar. Coast Shelf S* 53 (6), 759–778.
- Mason, D., Scott, T., Dance, S., 2010. Remote sensing of intertidal morphological change in Morecambe Bay, UK between 1991 and 2007. *Estuar. Coast Shelf S* 87 (3), 487–496.
- McFeeters, S.K., 1996. The use of the Normalized Difference Water Index (NDWI) in the delineation of open water features. *Int. J. Remote Sens.* 17 (7), 1425–1432.
- Morris, R.L., Konlechner, T.M., Ghisalberti, M., Swearer, S.E., 2018. From grey to green: Efficacy of eco-engineering solutions for nature-based coastal defence. *Glob. Chang. Biol.* 24 (5), 1827–1842.
- Murray, N.J., Worthington, T.A., Bunting, P., Duce, S., Hagger, V., Lovelock, C.E., Lucas, R., Saunders, M.I., Sheaves, M., Spalding, M., 2022. High-resolution mapping of losses and gains of Earth’s tidal wetlands. *Science* 376 (6594), 744–749.
- Ni, R., Tian, J., Li, X., Yin, D., Li, J., Gong, H., Zhang, J., Zhu, L., Wu, D., 2021. An enhanced pixel-based phenological feature for accurate paddy rice mapping with Sentinel-2 imagery in Google Earth Engine. *ISPRS J. Photogramm. Remote Sens.* 178, 282–296.
- Nienhuis, J.H., Ashton, A.D., Edmonds, D.A., Hoitink, A., Kettner, A.J., Rowland, J.C., Törnqvist, T.E., 2020. Global-scale human impact on delta morphology has led to net land area gain. *Nature* 577 (7791), 514–518.
- Otsu, N., 1979. A threshold selection method from gray-level histograms. *IEEE Trans. Syst. Man Cybern. Syst.* 9 (1), 62–66.
- Rossington, K., Spearman, J., 2009. Past and future evolution in the Thames Estuary. *Ocean Dyn.* 59 (5), 709–718.
- Ryu, J.-H., Kim, C.-H., Lee, Y.-K., Won, J.-S., Chun, S.-S., Lee, S., 2008. Detecting the intertidal morphologic change using satellite data. *Estuar. Coast Shelf S* 78 (4), 623–632.
- Sagar, S., Roberts, D., Bala, B., Lymburner, L., 2017. Extracting the intertidal extent and topography of the Australian coastline from a 28 year time series of Landsat observations. *Remote Sens. Environ.* 195, 153–169.
- Salameh, E., Frappart, F., Almar, R., Baptista, P., Heygster, G., Lubac, B., Raucoules, D., Almeida, L.P., Bergsma, E.W., Capo, S., 2019. Monitoring beach topography and nearshore bathymetry using spaceborne remote sensing: a review. *Remote Sens.* 11 (19), 2212.
- Salameh, E., Frappart, F., Turki, I., Laignel, B., 2020. Intertidal topography mapping using the waterline method from Sentinel-1 & -2 images: the examples of Arcachon and Veys Bays in France. *ISPRS J. Photogramm. Remote Sens.* 163, 98–120.
- Salameh, E., Frappart, F., Desroches, D., Turki, I., Carbonne, D., Laignel, B., 2021. Monitoring intertidal topography using the future SWOT (Surface Water and Ocean Topography) mission. *Remote Sens. Appl. Soc. Environ.* 23, 100578.
- Seale, C., Redfern, T., Chatfield, P., Luo, C., Dempsey, K., 2022. Coastline detection in satellite imagery: a deep learning approach on new benchmark data. *Remote Sens. Environ.* 278, 113044.
- Tan, K., Chen, J., Zhang, W., Liu, K., Tao, P., Cheng, X., 2020. Estimation of soil surface water contents for intertidal mudflats using a near-infrared long-range terrestrial laser scanner. *ISPRS J. Photogramm. Remote Sens.* 159, 129–139.
- Temmerman, S., Meire, P., Bouma, T.J., Herman, P.M.J., Ysebaert, T., De Vriend, H.J., 2013. Ecosystem-based coastal defence in the face of global change. *Nature* 504 (7478), 79–83.
- Tian, J., Wang, L., Yin, D., Li, X., Diao, C., Gong, H., Shi, C., Menenti, M., Ge, Y., Nie, S., 2020. Development of spectral-phenological features for deep learning to understand *Spartina alterniflora* invasion. *Remote Sens. Environ.* 242, 111745.
- Tong, S.S., Deroin, J.P., Pham, T.L., 2020. An optimal waterline approach for studying tidal flat morphological changes using remote sensing data: A case of the northern coast of Vietnam. *Estuar. Coast Shelf S*, 236.
- Tseng, K.-H., Kuo, C.-Y., Lin, T.-H., Huang, Z.-C., Lin, Y.-C., Liao, W.-H., Chen, C.-F., 2017. Reconstruction of time-varying tidal flat topography using optical remote sensing imageries. *ISPRS J. Photogramm. Remote Sens.* 131, 92–103.
- Tucker, C.J., 1979. Red and photographic infrared linear combinations for monitoring vegetation. *Remote Sens. Environ.* 8 (2), 127–150.
- Van der Wal, D., Pye, K., 2004. Patterns, rates and possible causes of saltmarsh erosion in the Greater Thames area (UK). *Geomorphology* 61 (3–4), 373–391.

- Van Der Wal, D., Pye, K., Neal, A., 2002. Long-term morphological change in the Ribble Estuary, northwest England. *Mar. Geol.* 189 (3–4), 249–266.
- Vos, K., Harley, M.D., Splinter, K.D., Simmons, J.A., Turner, I.L., 2019. Sub-annual to multi-decadal shoreline variability from publicly available satellite imagery. *Coast Eng.* 150, 160–174.
- Wang, Y., Liu, Y., Jin, S., Sun, C., Wei, X., 2019. Evolution of the topography of tidal flats and sandbanks along the Jiangsu coast from 1973 to 2016 observed from satellites. *ISPRS J. Photogramm. Remote Sens.* 150, 27–43.
- Wang, X., Xiao, X., Zou, Z., Chen, B., Ma, J., Dong, J., Doughty, R.B., Zhong, Q., Qin, Y., Dai, S., Li, X., Zhao, B., Li, B., 2018. Tracking annual changes of coastal tidal flats in China during 1986–2016 through analyses of Landsat images with Google Earth Engine. *Remote Sens. Environ.*
- Wu, W., Zhi, C., Gao, Y., Chen, C., Chen, Z., Su, H., Lu, W., Tian, B., 2022. Increasing fragmentation and squeezing of coastal wetlands: Status, drivers, and sustainable protection from the perspective of remote sensing. *Sci. Total Environ.* 811, 152339.
- Xie, W.M., He, Q., Zhang, K.Q., Guo, L.C., Wang, X.Y., Shen, J., Cui, Z., 2017. Application of terrestrial laser scanner on tidal flat morphology at a typhoon event timescale. *Geomorphology* 292, 47–58.
- Xie, W., Wang, X., Guo, L., He, Q., Dou, S., Yu, X., 2021. Impacts of a storm on the erosion process of a tidal wetland in the Yellow River Delta. *Catena* 205, 105461.
- Xu, H., 2006. Modification of normalised difference water index (NDWI) to enhance open water features in remotely sensed imagery. *Int. J. Remote Sens.* 27 (14), 3025–3033.
- Yamano, H., Shimazaki, H., Matsunaga, T., Ishoda, A., McClennen, C., Yokoki, H., Fujita, K., Osawa, Y., Kayanne, H., 2006. Evaluation of various satellite sensors for waterline extraction in a coral reef environment: Majuro Atoll, Marshall Islands. *Geomorphol.* 82 (3–4), 398–411.
- Yang, Z., Wang, L., Sun, W., Xu, W., Tian, B., Zhou, Y., Yang, G., Chen, C., 2022. A new adaptive remote sensing extraction algorithm for complex muddy coast waterline. *Remote Sens.* 14 (4), 861.
- Zhang, S., Xu, Q., Wang, H., Kang, Y., Li, X., 2022. Automatic Waterline Extraction and Topographic Mapping of Tidal Flats From SAR Images Based on Deep Learning. *Geophys Res Lett*, 49 2 e2021GL096007.
- Zhang, K., Gann, D., Ross, M., Robertson, Q., Sarmiento, J., Santana, S., Rhome, J., Fritz, C., 2019. Accuracy assessment of ASTER, SRTM, ALOS, and TDX DEMs for Hispaniola and implications for mapping vulnerability to coastal flooding. *Remote Sens. Environ.* 225, 290–306.
- Zou, Z., Dong, J., Menarguez, M.A., Xiao, X., Qin, Y., Doughty, R.B., Hooker, K.V., Hambright, K.D., 2017. Continued decrease of open surface water body area in Oklahoma during 1984–2015. *Sci. Total Environ.* 595, 451–460.